Effects of H_2O-CO_2 Fluids, Temperature, and Peridotite Fertility on Partial Melting in Mantle Wedges and Generation of Primary Arc Basalts

Michael Lara[1,2,*]

Rajdeep Dasgupta[2]

[1]Department of Earth and Environmental Sciences, University of Minnesota, 116 Church St SE, Minneapolis, MN 55455, USA

[2]Department of Earth, Environmental and Planetary Sciences, Rice University, 6100 Main Street, MS 126, Houston, TX 77005, USA.

*Corresponding author: mlara@umn.edu

Abstract

Many lines of evidence from high *P-T* experiments, thermodynamic models, and natural observations suggest that slab-derived aqueous fluids, which flux mantle wedges contain variable amounts of dissolved CO_2. However, constraints on the effects of H_2O-CO_2 fluids on mantle melting, particularly at mantle wedge *P-T* conditions, are limited. Here we present new piston cylinder experiments using $Au_{75}Pd_{25}$ capsules on fertile and depleted peridotite compositions with 3.5 wt.% H_2O and XCO_2 [= molar CO_2 / (CO_2 + H_2O)] of 0.04-0.17. Experiments were performed at 2-3 GPa and 1350 °C to assess how temperature, peridotite fertility, and XCO_2 of slab-derived fluid affects partial melting in mantle wedges. All experiments produce olivine + orthopyroxene + 7 to 41 wt.% partial melt. Our new data, along with previous lower temperature data, show that as mantle wedge temperature increases, primary melts become richer in SiO_2, FeO* and MgO and poorer CaO, Al_2O_3 and alkalis when influenced by H_2O-CO_2 fluids. At constant *P-T* and bulk H_2O content, the extent of melting in the mantle wedge is largely controlled by peridotite fertility and XCO_2 of slab-fluid. High XCO_2 depleted compositions generate ~ 7 wt.% melt whereas, at identical *P-T*, low XCO_2 fertile compositions generate ~ 30-40 wt.% melt. Additionally, peridotite fertility and XCO_2 have significant effects on peridotite partial melt compositions. At a constant *P-T*-XCO_2, fertile peridotites generate melts richer in CaO and Al_2O_3 and poorer in SiO_2, MgO+FeO, and alkalis. Similar to previous experimental studies, at a constant *P-T*-fertility condition, as XCO_2 increases, SiO_2 and CaO of melts systematically decrease and increase, respectively. Such distinctive effects of oxidized form of dissolved carbon on peridotite partial melt compositions are not observed if the carbon-bearing fluid is reduced, such as CH_4-bearing. Considering the large effect of XCO_2 on melt SiO_2 and

CaO concentrations and the relatively oxidized nature of arc magmas, we compare the SiO_2/CaO of our experimental melts and melts from previous peridotite + H_2O ± CO_2 studies to the SiO_2/CaO systematics of primitive arc basalts and ultra-calcic, silica-undersaturated arc melt inclusions. From this comparison, we demonstrate that across most *P*-*T*-fertility conditions predicted for mantle wedges, partial melts from bulk compositions with $XCO_2 \geq 0.11$ have lower SiO_2/CaO than all primitive arc melts found globally, even when correcting for olivine fractionation, whereas partial melts from bulk compositions with $XCO_2 = 0.04$ overlap the lower end of the SiO_2/CaO field defined by natural data. These results suggest that the upper XCO_2 limit of slab-fluids influencing primary arc magma formation is $0.04 < XCO_2 < 0.11$, and this upper limit is likely to apply globally. Lastly, we show that the anomalous SiO_2/CaO and CaO/Al_2O_3 signatures observed in ultra-calcic arc melt inclusions can be reproduced by partial melting of either CO_2-bearing hydrous fertile and depleted peridotites with $0 < XCO_2 < 0.11$ at 2-3 GPa, or from nominally CO_2-free hydrous fertile peridotites at P > 3 GPa.

Keywords: Arc magmatism; H_2O-CO_2 fluids; Hydrous peridotite melting; Mantle wedge; Ultra-calcic melt inclusions

INTRODUCTION

It is well accepted that hydrous fluids released from subducting oceanic lithosphere at sub-arc depths (60-120 km) significantly decrease the peridotite solidus and trigger partial melting in the mantle wedge generating primary arc magmas (e.g., Yoder & Tilley, 1962; Mysen & Boettcher, 1975; Ulmer, 2001; Grove *et al*., 2006; Spandler & Pirard, 2013). However, the physical and chemical conditions prevailing in mantle wedges during primary arc magma formation, i.e., slab-derived fluid composition, ambient mantle wedge composition, temperature, and pressure, are all predicted to vary within the global range of subduction zones (Figure 1); each parameter having a significant effect on primary arc magma composition. Therefore, successful models of primary arc magma formation must evaluate how peridotite partial melt compositions are predicted to vary across the range of predicted thermochemical conditions of mantle wedges globally. In turn, comparing experimental melts produced under controlled conditions to natural primitive arc melts may further constrain the environment of the sub-arc mantle during primary arc magma formation.

Slab-derived fluids fluxing mantle wedges are generally thought to be dominated by H_2O due to the preferential breakdown of hydrous minerals relative to carbonates at sub arc depths (Kerrick & Connolly 1998, 2001a,b; Molina & Polli, 2000; Gormann *et al*., 2006). Consequently, most previous experimental studies have envisioned mantle wedge fluxing agents as a nominally CO_2-free hydrous fluid or silicate melt (Ulmer, 2001; Till *et al*., 2012; Grove *et al*., 2012; Mitchell & Grove, 2015; Mallik *et al*., 2015, 2016; Grove & Till, 2019; Lara & Dasgupta, 2020). However, several studies demonstrate that variable amounts of carbonates and/or graphite may be dissolved by aqueous fluids or slab-derived melts that derive from the

slab, thereby introducing CO_2 at sub arc depths (Connolly, 2005; Gorman *et al*., 2006; Grassi & Schmidt, 2011; Tsuno & Dasgupta, 2012; Ague & Nicolescu, 2014; Kelemen & Manning, 2015; Duncan & Dasgupta, 2014, 2015, 2017; Tumiati *et al*., 2017, 2022; Martin & Hermann, 2018; Menzel *et al*., 2020; Farsang *et al*., 2021). The extent of carbon release from the slab also varies as a function of slab *P-T* paths (e.g., Dasgupta, 2013; Duncan & Dasgupta, 2017; Eguchi & Dasgupta, 2022), with hotter slabs causing greater carbon release. Indeed, natural slab-derived fluids undoubtedly contain variable amounts of dissolved carbonates as evidenced in fluid inclusion, melt inclusion, isotope, and arc xenolith studies (Wallace, 2005; Ducea *et al*., 2005; de Leeuw *et al*., 2007; Sapienza *et al*., 2009; Blundy *et al*., 2010; Frezzotti *et al*., 2011; Liu *et al*., 2022). However, even among studies suggesting significant slab-CO_2 liberation, debate remains on the depth of CO_2 release, i.e., fore-arc versus sub-arc depths (e.g., Stewart & Ague, 2020), with some studies outlining possibility of carbonatitic melt release from subduction zone environment much deeper than typical sub-arc depths (e.g., Thomsen & Schmidt, 2008; Tsuno *et al*., 2012; Thomson *et al*., 2016). However, even if released, slab-derived CO_2 may form metasomatic carbonates upon interaction with peridotite near the slab/wedge interface (Saha & Dasgupta, 2019; Sun & Dasgupta, 2019; Kelemen *et al*., 2022), preventing some CO_2 from fluxing the core of the mantle wedge where partial melting commences. Hence, an independent measure of CO_2 transfer from slab to arc melt source region is necessary.

Experimental studies have demonstrated that both H_2O and CO_2 have significant yet contrasting effects on peridotite partial melt compositions (e.g., Hirose, 1997a,b; Gaetani & Grove, 1998; Dasgupta *et al*., 2007; Lara & Dasgupta, 2022). Most notably, the SiO_2 and CaO concentrations of peridotite partial melts generated at 2-3 GPa depend strongly on the CO_2 concentration of slab-fluid added, hereafter written in terms of XCO_2 [= molar CO_2 / (CO_2 +

H_2O)], and this dependence becomes amplified as the solidus is approached (Figure 2). In contrast, the SiO_2 and CaO concentrations of dry peridotite partial melts at 1-3 GPa remain relatively constant from 0-45% melting (Figure 2). Thus, XCO_2 of slab fluid that reaches the core of the mantle wedge is predicted to have greatest effect on primary arc melt compositions.

Because most experimental studies in peridotite + H_2O + CO_2 systems with reported partial melt compositions are run at pressures ≥ 4 GPa (Brey *et al*., 2009; Foley *et al*., 2009; Dvir & Kessel, 2017), the effects of H_2O-CO_2 fluids on peridotite melting at shallower pressures (1-3 GPa) relevant for mantle wedges is still largely unconstrained. A recent experimental melting study at 1200 °C and 2-4 GPa showed that depleted peridotite + H_2O-CO_2 fluids with XCO_2 > 0.10 produce melts, which are too SiO_2 poor and CaO-rich to match primitive arc magmas found globally (Figure 2), thereby setting an upper XCO_2 limit of fluids in primary arc melt source regions (Lara & Dasgupta 2022). However, for this limit to apply globally, further experimental investigation is needed over *P*-*T*-*X* space not considered in Lara & Dasgupta (2022) but known to prevail in mantle wedges. For example, minor element systematics in primitive arc basalts reflect large variations in mantle wedge thermal structures (Plank & Langmuir 1988; Turner & Langmuir 2015; Turner *et al*., 2016) while subduction zone thermal models predict a wide range of maximum mantle wedge temperatures, which far exceed 1200 °C (Syracuse *et al*., 2010; Perrin *et al*., 2018; Figure 1). Furthermore, primitive arc magmas display considerable variations in trace element and isotope ratios, which are largely independent of slab inputs (eg. La/Sm, Dy/Yb, $^{143}Nd/^{144}Nd$, $^{176}Hf/^{177}Hf$), leading several authors to conclude that heterogeneity in the mantle wedge is not only controlled by variable addition of a slab component, but also by variable melt depletion in the mantle wedge before the addition of slab components (Turner & Langmuir 2022b; Turner *et al*., 2017; Woodhead *et al*., 2012; Tollstrup 2010; Pearce *et al*.,

2007). This heterogeneity is also reflected in the major element systematics of sub-arc peridotite xenoliths, which follow a melt depletion trend ranging from fertile lherzolites to depleted harzburgites (Figure 1).

Here, we present the melting phase relations of fertile and depleted peridotite compositions in the presence of H_2O-CO_2 fluids ranging in XCO_2 from 0.04 to 0.17 at 2-3 GPa and 1350 °C. The goal was to expand the experimental conditions over which peridotite partial melt is generated in H_2O-CO_2 fluid-fluxed mantle wedge scenarios to account for the wide range of temperatures and peridotite fertility conditions predicted for mantle wedges globally. Given arc magmas are known to be relatively oxidized (e.g., Kelley & Cottrell, 2009), we chiefly tested the possible role of oxidized carbon-bearing fluids on arc magma genesis. However, we also compare oxidized peridotite partial melt compositions from this study and previous studies with those that are generated under the influence of reduced COH fluids. We compare our experimental melts, along with previous depleted and fertile peridotite + $H_2O \pm CO_2$ studies at mantle wedge *P-T* conditions, to a global set of primitive arc magmas to constrain the XCO_2 limit of fluids that may impact arc magma generation. We also asses if melting of peridotite in the presence of low XCO_2 fluids can reproduce major element trends observed in ultra-calcic, silica undersaturated arc melt inclusions (Schiano, 2000).

METHODS

Starting materials

Three depleted peridotite compositions are modeled after peridotite xenolith (AVX-51) from the Kamchatka arc (Rapp *et al*., 1999) with 3.5 wt.% H_2O added. CO_2 was added in the proportion of 0.35, 1.05, and 1.75 wt.% to make the starting compositions DP.04, DP.11, and DP.17, achieving bulk XCO_2 of 0.04, 0.11 and 0.17, respectively (Table 1). The starting materials were synthesized using reagent grade oxides (SiO_2, Fe_2O_3, MnO, MgO), carbonates ($CaCO_3$, Na_2CO_3, K_2CO_3), hydroxides ($Al(OH)_3$, $Mg(OH)_2$), and hydrated magnesium carbonate ($Mg_2(CO_3)(OH)_2.3H_2O$). Extensive details of the synthesis of DP.04, DP.11, and DP.17, are given in Lara & Dasgupta (2022).

Two fertile peridotite compositions (FP.04, FP.17) are modeled after KLB-1 peridotite (Davis *et al*., 2009) with 3.5 wt.% H_2O added. CO_2 was added in the proportion of 0.35 and 1.75 wt.% to make starting compositions FP.04 and FP.17, achieving bulk XCO_2 of 0.04 and 0.17, respectively (Table 1). Fertile peridotite compositions were synthesized using natural KLB-1 powder, reagent grade oxides (SiO_2, FeO), hydroxides ($Mg(OH)_2$, $Al(OH)_3$), carbonates ($CaCO_3$, Na_2CO_3) and hydrated magnesium carbonate ($Mg_2(CO_3)(OH)_2.3H_2O$). KLB-1, SiO_2, FeO, and $CaCO_3$ powders were mixed in the proportions of the calculated starting compositions and ground under ethanol for 1 h in an agate mortar. The mixtures were then fired in a Deltech CO-CO_2 gas mixing furnace at $\log fO_2 \sim$ FMQ – 2 for 24 h to decarbonate $CaCO_3$ and reduce any Fe^{3+} to Fe^{2+}. After reduction, $Mg(OH)_2$, $Al(OH)_3$, Na_2CO_3, and ($Mg_2(CO_3)(OH)_2.3H_2O$) were added to yield the desired H_2O, CO_2, MgO, Al_2O_3, and Na_2O contents of FP.04 and FP.17 (Table 1). This mixture was then ground under ethanol for 1 h in an agate mortar, collected in a glass vial and stored at a drying oven at 110 °C.

Experimental procedure

Experiments were performed at 2-3 GPa and 1350 °C using a half-inch piston cylinder apparatus in the Experimental Petrology Laboratory at Rice University. Starting mixes were packed into 3 mm outer diameter $Au_{75}Pd_{25}$ capsules and experiments were performed using a half-inch BaCO3/MgO pressure media following calibration and procedure from Tsuno & Dasgupta (2011). The temperature of each experiment was controlled and monitored using a Type C thermocouple, accurate within ±10 °C accounting for the thermal gradient across the assembly. Similar calibration, assembly, and capsule alloy were employed in a number of previous hydrous experimental studies from this laboratory (e.g., Duncan & Dasgupta, 2015; Carter & Dasgupta, 2018).

Experiments were run for durations of 69-139 h and were terminated by cutting off power to the heater and the assemblies were decompressed slowly. The capsules were retrieved from the assembly, mounted in Petropoxy 154 and stored in a furnace at 100 °C for 1 h to harden. The mounted capsules was first ground on a 600 grit SiC paper to expose the synthesized samples. Once the capsules were opened, the samples were impregnated with a low viscosity Petropoxy 154 under vacuum to prevent pluck outs and loss of material from the capsule upon further polishing. The impregnated samples were then polished on a nylon cloth with 3 and 1 micron diamond powder and without the use of any lubricant. To get rid of polishing debris and avoid contaminating the polishing pads for finer polishing, samples were repeatedly cleaned using compressed air.

Analysis of experiments

Polished samples were first carbon coated and then analyzed using a field emission gun electron microprobe (JEOL JXA-8530F Hyperprobe) at the Department of Earth, Environmental and Planetary Sciences at Rice University. Minerals and melts were identified using a combination of textural analyses using BSE images and energy dispersive X-ray spectroscopy (EDS) and analyzed for major elements using wavelength dispersive X-ray spectroscopy (WDS) at an accelerating voltage of 15 kV. Minerals were analyzed using fully focused, 20 nA electron beam. Melts were analyzed using a 10 nA defocused electron beam with beam sizes of 10-50 μm. Analytical standards used for silicate minerals were jadeite (Na), chrome diopside (Si, Ca, Mg), biotite (K), olivine (Mg, Si, Fe), rutile (Ti), almandine (Si, Al), plagioclase (Si, Ca, Al), and rhodonite (Mn) whereas the melt phase was analyzed using a basaltic glass standard NMNH-113716-1. Large defocused beam analyses were performed evenly across each melt pool to ensure that our analyses capture average melt compositions and were not biased by heterogeneously distributed melt quench products.

RESULTS

Phase assemblage and textures

Phase assemblages and proportions are listed in Table 2, back-scattered electron images of experimental products are shown in Figure 3 and mineral compositions reported in Tables 3-4. All experiments in this study had a phase assemble of olivine + orthopyroxene + melt. Olivines are euhedral with diameters typically >100 μm and in all experiments appear adjacent to the melt pool (Figure 3). Orthopyroxenes are also euhedral but with diameters <50 μm and in all

experiments appear on the opposite side of the capsule relative to the melt pool (Figure 3). Similar gradients in mineralogy are observed in many peridotite + $H_2O \pm CO_2$ studies and are attributed to the thermal compaction effects facilitated by the presence of melt, a small thermal gradient, and long experimental run durations (e.g., Lesher & Walker, 1998; Grove *et al*., 2006; Till *et al*., 2012; Lara & Dasgupta, 2022). Two types of melt textures were observed in experimental run products. The melt phase in most experiments consists of an aggregate of metastable quench crystals, which form rapidly upon quenching volatile-rich melts (Green 1973, 1976). This texture ranges from a nearly homogeneous distributions of quench products (Figure 3B) to a more heterogeneous distribution where large quench products are surrounded by a matrix of finer grained material (Figure 3D). The second melt texture was observed in two fertile peridotite experiments, which produced smooth and glassy melt (Figure 3F). These experiments produced significantly higher melt fractions relative to depleted peridotite experiments (Table 5) and therefore, having lower melt volatile contents, likely facilitated the formation of silicate glass.

Melt compositions

Varying amounts of Fe transfer from our experimental product to the $Au_{75}Pd_{25}$ capsules occurred during each experiment resulting in Fe-loss ranging from 1.7 to 31 % (Table 2). A similar degree of Fe-loss is reported in previous hydrous peridotite studies (e.g., Gaetani and Grove, 1998; Mallik *et al*., 2015). We have corrected our analyzed melt compositions, excluding B534 and B513, which showed minimal Fe loss (Table 2), using methods of Mallik *et al*. (2015). The Fe-

252 corrected melt compositions along with the two uncorrected partial melt compositions are given
253 in Table 5 and plotted in Figure 4.
254 In the depleted peridotite experiments, SiO_2 concentrations of melts decrease from 50 to
255 44 wt.% at 2 and 3 GPa with increasing bulk XCO_2 (Figure 4). Melt CaO concentrations also
256 show strong positive correlations with bulk XCO_2 where they increase from 8 to 13 wt.% at 2
257 GPa and from 4 to 9 wt.% at 3 GPa. Al_2O_3 concentrations show much less variability with
258 increasing bulk XCO_2 as all depleted peridotite partial melts have ~ 4-5 wt.% Al_2O_3. MgO
259 concentrations are nearly constant across the bulk XCO_2 interval at a given pressure, where 2
260 GPa melts have on average ~ 24 wt.% MgO and 3 GPa melts have ~ 27 wt.% MgO. FeO*
261 concentrations at 2 GPa remain constant ~ 11-12 wt.% while at 3 GPa, FeO* concentrations
262 show a systematic increase from ~12 to 14 wt.% as bulk XCO_2 increases.
263 In the fertile peridotite experiments, as XCO_2 increases, SiO_2 concentrations of partial
264 melts decrease from 48 to 43 wt.% at 2 GPa and from 44 to 38 wt.% at 3 GPa. CaO
265 concentrations increase from 8 to 16 wt.% at 2 GPa and from 11 to 14 wt.% at 3 GPa. Al_2O_3
266 concentrations increase from 9 to 10 wt.% at 3 GPa and decrease from 10.5 to 9 wt.% at 3 GPa.
267 MgO concentrations decrease from 22 to 19 wt.% at 2 GPa and increase from 22 to 26 wt.% at 3
268 GPa. FeO* concentrations remain ~10 wt.% at 2 GPa and increase to 11-11.5 wt.% at 3 GPa.
269 Lastly, $Na_2O + K_2O$ remains relatively constant between 1.0 and 1.5 wt.% at 2 and 3 GPa.
270
271 **Approach to chemical equilibrium**
272
273 Reversal experiments were not performed; however, the following criteria are used to establish
274 maintenance of a closed system and approach to equilibrium. (a) $K_{D_{Melt}}^{Ol}$ = 0.28 – 0.32 for all

experiments (Table 5), in excellent agreement with this exchange coefficient at equilibrium (Roeder & Emslie, 1970; Toplis, 2005; Filiberto & Dasgupta, 2011). (b) Long experimental duration of 69-139 h, similar to previous peridotite + H_2O ± CO_2 melting studies demonstrating equilibrium at similar *P-T* conditions (e.g., Dvir & Kessel, 2017, Lara & Dasgupta, 2022). (c) Small compositional heterogeneity in mineral WDS analyses (Tables 3-4). (d) Low sum of squared residuals in all experiments as demonstrated in mass balance calculations on an FeO*-free basis (Table 2).

DISCUSION

Effect of temperature on melting in a mantle wedge fluxed by H_2O-CO_2 fluids

To evaluate the effect of the temperature on the partial melting in an H_2O-CO_2 fluid fluxed mantle wedge, we compare our depleted peridotite-derived partial melts produced at 1350 °C with those from Lara & Dasgupta (2022), which used identical bulk compositions at 1200 °C (Figures 5 and 6).

From this comparison, it is observed that increasing temperature in peridotite + H_2O + CO_2 systems has a large effect on all major oxide concentrations in partial melts. The general trend observed at 2 and 3 GPa is that increase in temperature produces larger melt fractions relatively enriched in SiO_2 and FeO+MgO and depleted in CaO, Al_2O_3 and Na_2O+K_2O (Figures 5 and 6). The observed melting systematics are readily explained by the known effects of H_2O, CO_2, and temperature on peridotite partial melt compositions. Volatile species are highly incompatible during partial melting, therefore the amount H_2O and CO_2 dissolved in silicate

298 melts will decrease by increasing temperature and melt fraction. Additionally, many
299 experimental studies on natural and simplified peridotite + CO_2 systems have shown that melt
300 CaO is positively correlated while melt SiO_2 is negatively correlated with the amount of CO_2
301 dissolved in melt, irrespective of the nominal to moderate concentrations of H_2O in the melt
302 (Eggler, 1978; Gudfinnsson & Presnall, 2005; Dasgupta *et al*., 2007; Ghosh *et al*., 2014; Sun &
303 Dasgupta, 2019; Dasgupta *et al*., 2022). While our starting compositions contain significant
304 amounts H_2O, it has been demonstrated that CO_2 has a dominating effect on peridotite partial
305 melt compositions in mixed H_2O-CO_2 systems, even at low XCO_2 (Figure 1; Lara & Dasgupta
306 2022). Thus, increasing temperature at a constant bulk composition or decreasing bulk XCO_2 at a
307 constant temperature should diminish the amount of CO_2 dissolved in silicate melts, producing
308 more SiO_2-rich and CaO-poor melts. This is well exemplified in Figure 5 where the most SiO_2-
309 poor, CaO-rich and lowest degree melts are produced at XCO_2=0.17 and 1200 °C, while the
310 most SiO_2-rich, CaO-poor and highest degree melts are produced at XCO_2=0.04 and 1350 °C
311 (Figure 6).
312 Na_2O, K_2O, and Al_2O_3 all behave incompatibly between 1200 and 1350 °C due to the
313 lack of alkali-bearing or aluminous phases like spinel, cpx or garnet in equilibrium with the
314 melts. These concentrations therefore decrease with increasing temperature. Partitioning of MgO
315 between minerals and melt is highly temperature-dependent in dry, hydrous, and carbonated
316 peridotite systems, resulting in higher MgO partial melts at higher temperatures (Kinzler &
317 Grove, 1992; Hirose & Kushiro, 1993; Gaetani & Grove, 1998; Dasgupta *et al*., 2007; Mallik &
318 Dasgupta, 2013, 2014). Melt FeO* concentrations show a similar temperature dependence in dry
319 and hydrous systems; however, in carbonated peridotite systems, melt FeO* decreases with
320 increasing temperature (Dasgupta *et al*., 2007). Partial melts derived from peridotites fluxed by

low XCO_2 fluids, as envisioned in this study and Lara & Dasgupta (2022), become richer in both MgO and FeO* as temperature increases (Figures 5 and 6), similar to dry and hydrous peridotite systems. Conversely, partial melts of peridotite fluxed by high XCO_2 fluids show little correlation between FeO*, MgO, and temperature (Foley *et al*., 2009).

Effect of peridotite fertility and XCO_2 on extent of melting in mantle wedges

The effect of peridotite fertility on mantle melting has predominantly been discussed in the context of MORB generation inferred from volatile-free peridotite melting experiments and thermodynamic models (Wasylenki *et al*., 2003; Schwab & Johnston, 2001; Hirschmann, 2000; Hirschmann *et al*., 1998). These studies demonstrate that, at a constant *P-T*, fertile peridotites generate higher melt fractions relative to depleted peridotites due a combination of lower solidi temperatures and higher isobaric melt productivities (IMP). A similar relationship between fertility and melt productivity is briefly noted in the 1.2 GPa hydrous peridotite melting study of Mitchell & Grove (2015), however; the effect of peridotite fertility deeper in the mantle wedge, particularly in the presence H_2O and H_2O-CO_2 mixed fluids is less understood. A positive correlation between bulk H_2O content and melt fraction in peridotite systems at a constant *P-T* is predicted by thermodynamic models (Hirschmann *et al*., 1999) and documented in several peridotite melting studies (Lara & Dasgupta, 2022,2020; Mallik *et al*., 2015, 2016; Mitchel & Grove 2015). Therefore, to isolate the effects of peridotite fertility and XCO_2 on melt fraction produced in the mantle wedge, we first evaluate melt fractions solely from this study, which all have constant bulk H_2O of 3.5 wt.%, in Figure 7a. In Figures 7b-d, we further compare these

results to peridotite + H_2O ± CO_2 studies conducted on both fertile ($CaO+Al_2O_3$ > 5 wt.%, Mg# < 90) and depleted ($CaO+Al_2O_3$ < 5 wt.%, Mg# > 90) compositions (Table 1).

At 1350 °C and 2-3 GPa, the extent of melting in peridotite + H_2O + CO_2 systems increases by increasing peridotite fertility or decreasing XCO_2 of the slab-derived fluid (Figure 7a). The effect of peridotite fertility on batch melt productivity can be explained by differences in mineral modes and stability between fertile and depleted peridotite throughout each respective melting interval. To demonstrate this, we compare the melting systematics from the hydrous peridotite experiments of Grove & Till (2019) and Lara & Dasgupta (2020), which were run at similar pressures (3-3.2 GPa), temperatures (1050-1250 °C) and bulk H_2O contents (3.5-4.2 wt.%) but used fertile (FP) and depleted peridotite (DP), respectively (Table 1, Figure 7b). At 1050-1075 °C, FP is characterized by abundant cpx and garnet modes compared to DP (Figures 7c & 7d). Furthermore, cpx and garnet contribute to the melting reactions in FP to at least 1150 °C, whereas these phases are completely exhausted from DP at 1050 -1100 °C, after which olivine is the only mineral contributing to melting (Figure 7). Because garnet and cpx are more fusable minerals relative to olivine, FP displays higher melt productivities relative to DP in this melting interval (Figure 7B). Although the experiments from this study were run at 1350 °C, where cpx and garnet are completely exhausted in both FP and DP experiments (Table 2), higher melt fractions in FP experiments likely reflect larger contributions from cpx and garnet in the FP batch melting reactions relative to the DP. DP experiments at 1350 °C also display higher olivine modes relative to FP experiments (Supplementary Figure 1; Table 2), suggesting that enhanced stability of olivine in DP experiments at high temperatures further contributes to their relatively low melt productivities.

The effect of XCO_2 on extent of melting, as observed in Figure 7A, may be explained by a decrease is melt productivity as XCO_2 increases, as demonstrated in Figure 7B. Additionally, lower melt fractions in H_2O-CO_2 bearing experiments could be due to differences in solidi locations between the H_2O-fluid saturated peridotite solidus (HPS) and the H_2O-CO_2 fluid-saturated solidi (HCPS) (Figure 8). At ~2 GPa, the HCPS is ~100 °C hotter than the HPS due to their positive and negative slopes from 1-2 GPa, respectively. Thus, ~2 GPa the solidi locations of our starting compositions are expected to increase with XCO_2, potentially explaining the observations in Figure 7A. However, between 2-3 GPa, the HCPS slope becomes negative, and the solidus sharply decreases as CO_2 becomes significantly more soluble in near solidus melts within this pressure interval (Dasgupta, 2018). At 3 GPa, the solidi location of the HPCS is comparable to the higher temperature HPS solidus of Green (1973) and ~200 °C hotter than the HPS solidus from Grove *et al*. (2006) and Till *et al*. (2012). Therefore, whether increasing XCO_2 at 3 GPa will increase solidus temperature will depend on the true location of the HPS.

Given the effects of peridotite fertility and XCO_2 on extent of melting discussed above and shown in Figure 7, it can be inferred that if temperature and bulk H_2O of the mantle wedge have limited variations, fertile peridotites fluxed by low XCO_2 fluids are expected to generate the highest melt fractions, while depleted peridotites fluxed by high XCO_2 fluids are expected to generate the lowest melt fractions.

Effects of peridotite fertility and XCO_2 on partial melt compositions generated in mantle wedges

387 The composition of peridotite partial melts is governed by the bulk composition of peridotite, melt
388 fraction, and the relative compatibility of oxides throughout the melting interval. Peridotite fertility
389 exerts an influence on both the initial composition and the melt fraction at a given *P*-*T*, creating
390 challenges in predicting differences between FP and DP partial melts in mantle wedges. In
391 addition, the introduction of H_2O-CO_2 fluids to mantle wedges significantly alters oxide
392 compatibility throughout the partial melting interval (Figure 2). As a result, predicting the
393 combined effects of peridotite fertility and XCO_2 on partial melt compositions generated in mantle
394 wedges requires careful consideration of these factors.

395 To address this issue, in Figure 9, we plot the major element compositions of our DP and
396 FP partial melts generated at 1350 °C as a function of extent of melting. Additionally, we compare
397 our results to peridotite + H_2O studies where FP and DP experiments were run at near identical P-
398 T conditions. Although DP + H_2O experimental studies are scarce, we utilize the only known
399 peridotite + H_2O study where both DP and FP compositions were employed (Mitchell and Grove
400 2015). Additionally, we incorporate peridotite + H_2O experiments from Grove & Till (2019) and
401 Lara & Dasgupta (2020), which simulate partial melting under comparable *P*-*T*-bulk H_2O
402 conditions but utilize FP and DP starting compositions, respectively (Table 1).

403 Observations of experiments in both H_2O and H_2O-CO_2 bearing systems reveal that SiO_2
404 concentrations of peridotite partial melts generated in mantle wedges can vary widely from 50-38
405 wt%, depending on peridotite fertility of XCO_2 of slab-derived fluid, and as high as 60 wt.% in
406 CO_2 free systems (Figure 9). The wide range of SiO_2 concentrations in experimental melts is
407 influenced by both fertility and XCO_2, as FP tends to generate lower melt SiO_2 concentrations than
408 DP at a given *P*-*T*, while increasing XCO_2 is associated with decreasing SiO_2 concentrations. The
409 effect of fertility on SiO_2 concentrations may in part be explained by higher olivine modes and

410 olivine/orthopyroxene ratios observed in DP residues relative to FP residues (Supplementary
411 Figure 1; Table 2), while the effect of XCO_2 on melt SiO_2 concentrations, as discussed previously,
412 is due to the well documented effect of dissolved CO_3^{2-} on peridotite partial melt compositions, in
413 addition to the role of dissolved carbonates in stabilizing more polymerized mineral phase such as
414 opx over olivine (e.g., Kushiro, 1975; Hirose, 1997b; Dasgupta *et al*, 2007; Mallik & Dasgupta,
415 2013; Sun & Dasgupta, 2019; Dasgupta *et al*., 2022).

416 Our experiments display two distinct CaO trends for DP and FP, both decreasing with
417 increasing melt fraction (Figure 9). The FP trend is offset to higher CaO concentrations relative to
418 the DP trend due to the higher initial CaO concentrations in FP (Table 1) and the lack of
419 clinopyroxene in both DP and FP residues (Table 2). In both FP and DP trends, higher XCO_2
420 experiments make up the lower degree and more CaO-rich melts, reflecting the effect of XCO_2 on
421 extent of melting as discussed in the previous section. In peridotite + H_2O experiments, there is no
422 clear trend relating peridotite fertility to melt CaO concentrations, however, there are distinct
423 differences in the overall melting trend relative to peridotite + H_2O. + CO_2 experiments. This
424 discrepancy is largely due to differences in the stability of clinopyroxene throughout the melting
425 intervals of the two systems. In peridotite + H_2O systems, clinopyroxene can be stable in the
426 residue up to 25 wt % partial melting (Grove & Till, 2019), generating low degree melts poor in
427 CaO which become more CaO-rich as melting degree increases (Figure 9). In contrast,
428 clinopyroxene is exhausted early in the melting interval in our experiments, due to the strong
429 affinity of Ca^{+2} cations with CO_3^{2-} dissolved in melt (Brooker *et al*., 2001; Dasgupta *et al*., 2007).

430 In our peridotite + H_2O + CO_2 experiments, FP partial melts are about 5 wt.% richer in
431 Al_2O_3 relative to DP, but neither trend shows a strong correlation with extend of melting (Figure
432 9). Conversely, in Peridotite + H_2O systems, Al_2O_3 behaves incompatibly in both FP and DP

433 experiments, resulting in low degree melts enriched in Al_2O_3 followed by a decrease in Al_2O_3 as
434 melting degree increases. One significant difference between peridotite + H_2O + CO_2 and
435 Peridotite + H_2O systems is that in the former, low degree melts are extremely poor in Al_2O_3
436 (<5wt.%) while in the later, low degree melts have Al_2O_3 >15 wt.%. This observation may further
437 be explained by the effect of melt CO_3^{2-} on the attraction of +2 cations (Ca, Mg, Fe) and
438 consequently, the dilution of +3 cations (Al). In contrast, low degree melts from CO_2-free
439 experiments are polymerized and enriched in +3 and +4 cations (Al and Si) and diluted with respect
440 to +2 cations Ca, Mg, and Fe (Figure 9).
441
442 **Effects of oxidized vs. reduced COH fluids on peridotite partial melt compositions**
443
444 Although the speciation of volatiles in our melts was not directly measured, CO_3^{2-} is inferred as
445 the dominant carbon species dissolved in our melts based the relationship between melt SiO_2, CaO
446 and XCO_2 (Figures 4 and 8). Additionally, fO_2 of un-buffered high-pressure hydrous peridotite
447 experiments run in Au-Pd capsules typically range from QFM-1 to QFM+2 (Mandler & Grove,
448 2016; Grove *et al*., 2006), and at these fO_2 and pressure conditions, CO_2 solubility models predict
449 that CO_3^{2-} is the dominant carbon species in basaltic melts (e.g., Holloway *et al*., 1992; Eguchi &
450 Dasgupta, 2018a). To further explore the effect of carbon speciation on hydrous peridotite partial
451 melt compositions, in Figure 10 we compare our FP partial melt compositions along with other FP
452 melts generated under oxidizing conditions near the QFM buffer where the dissolved carbon
453 species is predominantly CO_3^{2-} (Pinter *et al*., 2023; Dvir and Kessel, 2017; Foley *et al*., 2009;
454 Thibault *et al*., 1992; Wallace and Green, 1988) to partial melts produced under reducing

455 conditions near the iron-wüstite buffer where CH_4 is the dominant dissolved carbon species (Liu
456 *et al*., 2023; Litasov *et al*., 2014; Jakobsson & Holloway, 2008).

457 The results of this comparison demonstrate that while the melting trends of peridotite +
458 H_2O + CO_2 systems follow a distinct path, with low degree melts being SiO_2- and Al_2O_3-poor and
459 CaO-rich and becoming more SiO_2- and Al_2O_3-rich and CaO-poor as melting progresses, this trend
460 is not observed in reduced peridotite + H_2O + CH_4 systems (Figure 10). Rather, SiO_2, Al_2O_3, CaO
461 and MgO+FeO contents of reduced peridotite partial melts remain relatively constant throughout
462 the melting interval at a given XCH_4 (molar $CH_4/(CH_4+H_2O)$), suggesting both a lack of CO_3^{2-}
463 complexes dissolved in reduced basaltic melts and a weak effect of CH_4 on peridotite partial melt
464 compositions. Low degree melts (<10 wt.%) in peridotite + H_2O + CH_4 systems are poorer in SiO_2
465 and Al_2O_3 and richer in CaO and MgO compared to carbon-free peridotite + H_2O systems. This
466 may be explained by the presence of CH_4 decreasing the activity of H_2O (aH_2O) as high aH_2O
467 during peridotite partial melting, especially if the system is H_2O-fluid saturated, produces near-
468 solidus melts which are rich in SiO_2 and Al_2O_3 and poor in CaO and MgO+FeO (Gaetani & Grove,
469 1998; Pirard & Hermann 2015; Grove & Till 2019; Lara & Dasgupta 2020). The suppression of
470 aH_2O is further illustrated by the relationship between XCH_4 and partial melt compositions.
471 Notably, the most carbon-poor, reduced system (Liu *et al*., 2023) produces melts that overlap with
472 carbon-free peridotite + H_2O systems, whereas at higher XCH_4, partial melts deviate from the
473 SiO_2, CaO, Al_2O_3 and MgO+FeO melting trends defined by peridotite + H_2O systems. However,
474 these differences may also be attributed to lower experimental pressures in Liu *et al*. (2023) relative
475 to Jakobsson & Holloway (2008) and Litasov *et al*. (2014) (Figure 10). In summary, partial melting
476 of reduced peridotite in the presence of COH fluids at P <4 GPa is not expected to produce
477 distinctive peridotite partial melt compositions (i.e. carbonatites, kimberlites, high Mg# andesites)

as seen in oxidized peridotite systems (Dasgupta *et al*., 2007; Mitchell and Grove, 2015; Grove and Till, 2019; Sun & Dasgupta, 2019; Lara & Dasgupta, 2020, 2022).

Limit of carbon's involvement in primary arc magma formation

In this section, we compare melt compositions from this study and previous peridotite + H_2O ± CO_2 studies run at 2-3.5 GPa and with 2.5-4.2 wt.% bulk H_2O (Tenner *et al*., 2013; Grove & Till, 2019; Lara & Dasgupta, 2020, 2022) to the global dataset of primitive arc melts (PAM) from Schmidt & Jagoutz (2017) and to ultra-calcic, silica undersaturated melt inclusions (UCMI) sampled from Mt. Etna and the Luzon, Sunda and Vanuatu arcs (Kamenetsky and Clocchiatii, 1996; Schiano 2000; Kamenestsky *et al*., 2007; Elburg *et al*., 2007; Sorbadere *et al*., 2011). Because primitive arc magmas tend to be more oxidized than mid-ocean ridge and ocean island basalts, and even for the latter two the fO_2 conditions favor oxidized form of carbon (e.g., Stagno *et al*., 2013; Eguchi and Dasgupta, 2018b; Dasgupta *et al*., 2022), we restrict our comparison with natural magmas for oxidized experimental partial melts only.

To aptly compare high pressure experimental melts to PAMs and UCMIs sampled at the surface, we have subtracted olivine from experimental melts (Mg# ~ 0.79) until they reached Mg# = 0.69; in agreement with the average Mg# observed in PAMs and UCMIs (Schmidt & Jagoutz, 2017). Given the strong effects of temperature and XCO_2 on melt SiO_2 and CaO compositions (Figures 4, 5, 6, and 9), we utilize the SiO_2/CaO systematics of PAMs to constrain XCO_2 of fluids in PAM source regions up to 1350 °C, near the thermal maximum predicted for

mantle wedges (Figure 1). In addition, we assess if melting of peridotite in the presence of low XCO_2 fluids can reproduce the distinctive major element features of UCMIs.

A globally applicable upper XCO_2 limit of mantle wedge fluids

In a recent experimental study, Lara & Dasgupta (2022) investigated the effects of H_2O-CO_2 fluids on mantle wedge melting using the depleted peridotite starting compositions at 1200 °C. It was demonstrated that partial melting of depleted peridotite in the presence of H_2O-CO_2 with $XCO_2 > 0.10$ produce melts which, when corrected for olivine fractionation, are distinctly poorer in SiO_2 and richer in CaO than all PAMs; thereby setting an upper XCO_2 limit of fluids inducing melting in PAM source regions at 1200 °C. However, considering that maximum mantle wedge temperatures are predicted to far exceed 1200 °C (Figure 1) and that increasing temperature in peridotite + H_2O + CO_2 systems increases melt SiO_2 and decreases melt CaO (Figures 4&5), the global applicability of the XCO_2 limit derived from Lara & Dasgupta (2022) must further be evaluated at higher temperatures. In Figure 11, we demonstrate that, up to 1350 °C, partial melts derived from fertile and depleted peridotites with bulk $XCO_2 \geq 0.11$ have significantly lower SiO_2/CaO than all PAMs found globally. Furthermore, melts produced from peridotites with $XCO_2 = 0.04$ have SiO_2/CaO, which marginally intersect the bottom of the PAM data, suggesting an upper XCO_2 limit closer to 0.04 for PAM genesis. As XCO_2 decreases, SiO_2/CaO of experimental melts increase at any given MgO concentration, eventually matching the majority of PAMs at $XCO_2 < 0.04$. If temperatures are >1350 °C, then SiO_2/CaO of experimental melts is expected to increase (Figures 5 and 6) and may eventually overlap the SiO_2/CaO of PAMs. However, melt MgO concentrations at such high temperatures, even after correcting for

524 olivine fractionation, will likely be too high to match PAMs (Figure 11). Thus, the upper XCO_2
525 limit of fluids influencing PAM genesis in the mantle wedge is $0.04 < XCO_2 < 0.11$ and is likely
526 to hold across all *P*-*T*-fertility conditions prevailing in mantle wedges globally.
527 We noted before that for subduction zones globally, oxidized form of carbon is more
528 likely in arc basalt source regions. The discussions in the previous section demonstrate that under
529 such conditions, mantle-derived melt compositions are strongly sensitive to compositions of
530 mixed H_2O-CO_2 fluids, allowing us to place a strong constraint on the carbon content of the fluid
531 in the mantle source regions. However, such limit is not easily placed if carbon in the fluid is
532 present as methane rather than carbon dioxide. This is owing to the fact that for a wider range of
533 XCH_4 in the fluid, the melt major element oxide concentrations remain relatively unmodified
534 (Fig. 10). Therefore, arc magma chemistry may not be inconsistent with local presence of
535 reduced COH fluids in different parts of subduction factory (e.g., Song *et al*., 2009; Li, 2017;
536 Wang *et al*., 2022; Zhang *et al*., 2023). In fact, even if supplied as a CH_4-rich fluid from the slab,
537 oxidation of such fluid is possible in the wedge environment, leading to precipitation of
538 graphite/diamond and generation of H_2O, following the reaction -

539 $$CH_4\ (\text{fluid}) + O_2 = C\ (\text{graphite/diamond}) + 2H_2O\ (\text{fluid}) \quad (1)$$

540 The reaction above further suggests that reduced carbon-bearing fluid, if supplied as a
541 hydrogenated species, is unlikely to generate melt compositional signals that are discernible from
542 H_2O-only partial melting processes.
543
544 *Genesis of ultra-calcic, silica undersaturated arc melt inclusions*
545

While most primitive arc melts have SiO_2 >45 wt.% and CaO <12 wt.% (Schmidt and Jagoutz, 2017), a small subset of primitive, often olivine-hosted, melt inclusions are silica undersaturated with high CaO (>14 wt.%) and CaO/Al_2O_3 (>1) contents (Sorbadere *et al*., 2013). Although volumetrically insignificant, ultra-calcic melt inclusions (UCMI), after Kogiso & Hirschmann (2001), have a widespread occurrence and have been extensively discussed. UCMIs have been shown to deviate from experimental melts of dry mantle lherzolite at pressures <4 GPa and hydrous mantle lherzolite <2 GPa (Schiano *et al*., 2000; Medard *et al*., 2006). The origin of UCMIs has thus been attributed to high degree partial melting of amphibole and cpx-rich cumulates in the lower crust and upper mantle within arc environments, which agrees well with the major and minor element characteristics of UCMIs (Schiano *et al*., 2000; Medard *et al*., 2006; Sorbadere *et al*., 2011). An alternative hypothesis to their origin is partial melting of peridotite sources in the presence of CO_2-rich fluids (Della-Pasqua & Varne, 1997), which are known to produce CaO-rich and SiO_2-poor melts (e.g., Hirsoe, 1997; Dasgupta *et al*., 2007; Dasgupta, 2018). Other studies have demonstrated that peridotite + CO_2 experiments produce melts too SiO_2-Al_2O_3-poor and CaO-MgO-rich to explain UCMIs (Schiano *et al*., 2000; Sorbadere *et al*., 2013). However, these studies did not consider partial melting of peridotite in the presence of low XCO_2 hydrous fluids, which are demonstrated in this study and Lara & Dasgupta (2022) to generate CaO-rich and SiO_2-poor melts passing through the SiO_2/CaO field of UCMIs at XCO_2 = 0.04 in Figure 11. Similar to previous studies (Schiano *et al*., 2000; Medard *et al*., 2006), 2 GPa melts from nominally CO_2-free hydrous peridotites cannot reproduce the low SiO_2/CaO of UCMIs; however, high pressure (≥ 3 GPa) hydrous fertile peridotite melts from Grove & Till (2019) and Tenner *et al*. (2013), which have yet to be considered in the context of UCMI genesis, are shown to have relatively low SiO_2/CaO (Figure

11). Thus, high pressure (≥ 3GPa) melting of hydrous fertile peridotite in the absence of CO_2 may also produce low SiO_2/CaO melts akin to UCMIs.

To further evaluate if melting of peridotite in the presence of H_2O and H_2O-CO_2 mixed fluids can produce UCMIs, in Figure 12, we compare the CaO/Al_2O_3 systematics of PAMs and UCMIs, with experimental melts plotted in Figure 11. As XCO_2 increases, CaO/Al_2O_3 of experimental melts increases at any given MgO content (Figure 12). Nominally CO_2 free, hydrous fertile peridotite experiments at ≥ 3 GPa generate partial melts with relatively high CaO/Al_2O_3 of ~1, i.e., near the lower end of ultra-calcic melt inclusions, which may be attributed to enhanced stability of garnet in the residue producing melts with high CaO/Al_2O_3 (Tenner *et al*., 2013). Conversely, 3 GPa melts produced from CO_2 free hydrous depleted peridotites from Lara & Dasgupta (2020) have lower CaO/Al_2O_3 ratios overlapping the PAM field, but lower than UCMI, likely related to the lack of garnet in the residues of these experiments. Thus, in the absence of CO_2, UCMI formation is restricted to high pressure (> 3 GPa) hydrous melting of fertile, garnet-bearing peridotites. With XCO_2 increasing from 0.0 to 0.04, CaO/Al_2O_3 of experimental melts at 2 and 3 GPa overlap the CaO/Al_2O_3 of UCMIs (0.8-1.5), and with further increase in XCO_2 from 0.4 to 0.11, CaO/Al_2O_3 of experimental melts at 2 and 3 GPa exceeds that of UCMIs (Figure 11). Therefore, if UCMIs are formed by peridotite fluxed by slab-derived fluid at low pressures (<3 GPa), then their formation requires CO_2-bearing hydrous fluids with $0 < XCO_2 < 0.11$.

CONCLUSION

We performed high *P-T* experiments at 2-3 GPa and 1350 °C to constrain the effects of H_2O-CO_2 fluids, peridotite fertility and temperature on partial melting in the mantle wedge. Partial melts derived from depleted peridotite + H_2O + CO_2 systems at 2-3 GPa are shown to increase in SiO_2, MgO, and FeO* and decrease in CaO, Al_2O_3, and alkalis as temperature increases. Additionally, peridotite fertility and XCO_2 of slab-derived fluid are shown to have large effects on both the extent of melting and melt compositions generated in mantle wedges. We demonstrate that carbon dissolved as CO_3^{2-} in oxidized hydrous peridotite systems significantly affects partial melt compositions, while its effect is comparatively low in reduced peridotite systems where carbon dissolved as CH_4. Comparing the compositions of olivine fractionation corrected experimental melts from this study and others to primitive arc melts, we demonstrate that melts derived from depleted and fertile peridotite with bulk $XCO_2 > 0.04$ at 2-3 GPa and up to 1350 °C have lower SiO_2/CaO and higher CaO/Al_2O_3 than the global range of primitive arc melts and ultra-calcic melt inclusions. These findings suggest that slab-derived fluids, which influence primary arc basalt formation, have an upper XCO_2 limit falling within the range of $0.04 < XCO_2 < 0.11$.

Funding

This work was supported by NSF grant EAR-1763226 to R.D.

Acknowledgements

We sincerely thank two anonymous reviewers and the associate editor of the journal Dr. Carl Spandler for their reviews and comments. We also would like to acknowledge Rice University summer intern Elizabeth Mann for aiding in piston cylinder experiments.

References

Ague, J. J. & Nicolescu, S. (2014). Carbon dioxide released from subduction zones by fluid-mediated reactions. *Nature Geoscience*. **7**, 355–360.

Blundy, J., Cashman, K. V., Rust, A. & Witham, F. (2010). A case for CO2-rich arc magmas. *Earth and Planetary Science Letters*. **290**, 289–301.

Brooker, R.A., Kohn, S.C., Holloway, J.R., McMillan, P.F., (2001). Structural controls on the solubility of CO_2 in silicate melts Part II: IR characteristic of carbonate groups in silicate glasses. *Chemical Geology*. **174**, 241–254.

Carter, L. B. & Dasgupta, R. (2018). Decarbonation in the Ca-Mg-Fe carbonate system at mid-crustal pressure as a function of temperature and assimilation with arc magmas – Implications for long-term climate. *Chemical Geology*. **492**, 30–48.

Connolly, J. A. D. (2005). Computation of phase equilibria by linear programming: A tool for geodynamic modeling and its application to subduction zone decarbonation. *Earth and Planetary Science Letters*. **236**, 524–541.

Dasgupta, R. (2018). Volatile-bearing partial melts beneath oceans and continents–Where, how much, and of what compositions? *American Journal of Science*. **318**, 141–165.

Dasgupta, R., Chowdhury, P., Eguchi, J., Sun, C. & Saha, S. (2022). Volatile-bearing Partial Melts in the Lithospheric and Sub-Lithospheric Mantle on Earth and Other Rocky Planets. *Reviews in Mineralogy and Geochemistry*. **87**, 575–606.

Dasgupta, R., Hirschmann, M. M. & Smith, N. D. (2007). Partial melting experiments of peridotite + CO2 at 3 GPa and genesis of alkalic ocean island basalts. *Journal of Petrology*. **48**, 2093–2124.

Dasgupta, R. (2013). Ingassing, Storage, and Outgassing of Terrestrial Carbon through Geologic Time. *Reviews in Mineralogy and Geochemistry*. **75**, 183–229.

642 Davis, F. A., Tangeman, J. A., Tenner, T. J. & Hirschmann, M. M. (2009). The composition of
643 KLB-1 peridotite. *American Mineralogist* **94**, 176–180.

644 de Leeuw, G. A. M., Hilton, D. R., Fischer, T. P. & Walker, J. A. (2007). The He-CO2 isotope
645 and relative abundance characteristics of geothermal fluids in El Salvador and Honduras:
646 New constraints on volatile mass balance of the Central American Volcanic Arc. *Earth and*
647 *Planetary Science Letters*. **258**, 132–146.

648 Della-Pasqua, F. N. & Varne, R. (1997). Primitive ankaramitic magmas in volcanic arcs: A melt-
649 inclusion approach. *Canadian Mineralogist* **35**, 291–312.

650 Ducea, M. N., Saleeby, J., Morrison, J. & Valencia, V. A. (2005). Subducted carbonates,
651 metasomatism of mantle wedges, and possible connections to diamond formation: An
652 example from California. *American Mineralogist*. **90**, 864–870.

653 Duncan, M. S. & Dasgupta, R. (2014). CO_2 solubility and speciation in rhyolitic sediment partial
654 melts at 1.5-3.0GPa - Implications for carbon flux in subduction zones. *Geochimica et*
655 *Cosmochimica Acta* **124**, 328–347.

656 Duncan, M. S. & Dasgupta, R. (2015). Pressure and temperature dependence of CO_2 solubility in
657 hydrous rhyolitic melt: implications for carbon transfer to mantle source of volcanic arcs via
658 partial melt of subducting crustal lithologies. *Contributions to Mineralogy and Petrology*.
659 **169**, 54.

660 Duncan, M. S. & Dasgupta, R. (2017). Rise of Earth's atmospheric oxygen controlled by
661 efficient subduction of organic carbon. *Nature Geoscience*. **10**, 387–392.

662 Dvir, O. & Kessel, R. (2017). The effect of CO2 on the water-saturated solidus of K-poor
663 peridotite between 4 and 6 GPa. *Geochimica et Cosmochimica Acta*. **206**, 184–200.

664 Eggler, D. H. (1978). The effect of CO_2 upon partial melting of peridotite in the system Na_2O-
665 CaO-Al_2O_3) -MgO-SiO_2) -CO_2) to 35 kb, with an analysis of melting in a peridotite-H_2O-
666 CO_2) system. *American Journal of Science*. **278**, 305–343.

667 Eguchi, J. & Dasgupta, R. (2018a). A CO_2 solubility model for silicate melts from fluid
668 saturation to graphite or diamond saturation. *Chemical Geology*. **487**, 23–38.

669 Eguchi, J. & Dasgupta, R. (2018b). Redox state of the convective mantle from CO_2-trace
670 element systematics of oceanic basalts. *Geochemical Perspectives Letters* **8**, 17–21.

671 Eguchi, J. & Dasgupta, R. (2022). Cycling of CO_2 and H_2O constrained by experimental
672 investigation of a model ophicarbonate at deep subduction zone conditions. *Earth and*
673 *Planetary Science Letters*. **600**, 117866.

Elburg, M. A., Kamenetsky, V. S., Foden, J. D. & Sobolev, A. (2007). The origin of medium-K ankaramitic arc magmas from Lombok (Sunda arc, Indonesia): Mineral and melt inclusion evidence. *Chemical Geology* **240**, 260–279.

Falloon, T. J. & Green, D. H. (1989). The solidus of carbonated, fertile peridotite. *Earth and Planetary Science Letters*. **94**, 364–370.

Falloon, T. J. & Green, D. H. (1990). Solidus of carbonated fertile peridotite under fluid-saturated conditions. *Geology*. **18**, 195–199.

Farsang, S., Louvel, M., Zhao, C., Mezouar, M., Rosa, A. D., Widmer, R. N., Feng, X., Liu, J. & Redfern, S. A. T. (2021). Deep carbon cycle constrained by carbonate solubility. *Nature Communications*. **12**, 1–9.

Filiberto, J. & Dasgupta, R. (2011). Fe^{2+}-Mg partitioning between olivine and basaltic melts: Applications to genesis of olivine-phyric shergottites and conditions of melting in the Martian interior. *Earth and Planetary Science Letters* **304**, 527–537.

Foley, S. F., Yaxley, G. M., Rosenthal, A., Buhre, S., Kiseeva, E. S., Rapp, R. P. & Jacob, D. E. (2009). The composition of near-solidus melts of peridotite in the presence of CO_2 and H_2O between 40 and 60 kbar. *Lithos* **112**, 274–283.

Frezzotti, M. L., Selverstone, J., Sharp, Z. D. & Compagnoni, R. (2011). Carbonate dissolution during subduction revealed by diamond-bearing rocks from the Alps. *Nature Geoscience 2011*. **4**, 703–706.

Gaetani, G. A., Grove, T. L. & Bryan, W. B. (1993). The influence of water on the petrogenesis of subduction related igneous rocks. *Nature*. **365**, 332-334

Gaetani, G. A. & Grove, T. L. (1998). The influence of water on melting of mantle peridotite. *Contributions to Mineralogy and Petrology.* **131**, 323-346

Ghosh, S., Litasov, K. & Ohtani, E. (2014). Phase relations and melting of carbonated peridotite between 10 and 20 GPa: A proxy for alkali- and CO_2-rich silicate melts in the deep mantle. *Contributions to Mineralogy and Petrology* **167**, 1–23.

Gorman, P. J., Kerrick, D. M. & Connolly, J. A. D. (2006). Modeling open system metamorphic decarbonation of subducting slabs. *Geochemistry, Geophysics, Geosystems*. **7**.

Grassi, D. & Schmidt, M. W. (2011). The melting of carbonated pelites from 70 to 700 km depth. *Journal of Petrology*. **52**, 765–789.

Green, D. H. (1976). Experimental testing of "equilibrium" partial melting of peridodite under water-saturated, high pressure conditions. *Canadian Mineralogist*. **14**, 255-268

706 Green, D. H. (1973). Experimental melting studies on a model upper mantle composition at high
707 pressure under water-saturated and water-undersaturated conditions. *Earth and Planetary*
708 *Science Letters*. **19**, 37–53.

709 Grove, T. L., Chatterjee, N., Parman, S. W. & Médard, E. (2006). The influence of H_2O on
710 mantle wedge melting. *Earth and Planetary Science Letters*. **249**, 74–89.

711 Grove, T. L., Till, C. B. & Krawczynski, M. J. (2012). The role of H_2O in subduction zone
712 magmatism. *Annual Review of Earth and Planetary Sciences*. **40**, 413–439.

713 Grove, T. L. & Till, C. B. (2019). H_2O-rich mantle melting near the slab–wedge interface.
714 *Contributions to Mineralogy and Petrology*. **174**, 80.

715 Gudfinnsson, G. H. & Presnall, D. C. (2005). Continuous Gradations among Primary
716 Carbonatitic, Kimberlitic, Melilititic, Basaltic, Picritic, and Komatiitic Melts in Equilibrium
717 with Garnet Lherzolite at 3–8 GPa. *Journal of Petrology*. **46**, 1645–1659.

718 Hirose, K. & Kushiro, I. (1993). Partial melting of dry peridotites at high pressures:
719 Determination of compositions of melts segregated from peridotite using aggregates of
720 diamond. *Earth and Planetary Science Letters*. **114**, 477–489.

721 Hirose, K. (1997a). Melting experiments on lherzolite KLB-1 under hydrous conditions and
722 generation of high-magnesian andesitic melts. *Geology* **25**, 42.

723 Hirose, K. (1997b). Partial melt compositions of carbonated peridotite at 3 GPa and role of CO_2
724 in alkali-basalt magma generation. *Geophysical Research Letters*. Union **24**, 2837–2840.

725 Hirschmann, M. M., Ghiorso, M. S. & Stolper, E. M. (1999). Calculation of Peridotite Partial
726 Melting from Thermodynamic Models of Minerals and Melts. II. Isobaric Variations in
727 Melts near the Solidus and owing to Variable Source Composition. *Journal of Petrology*.
728 **40**, 297–313.

729 Hirschmann, M. M., Ghiorso, M. S., Wasylenki, L. E., Asimow, P. D. & Stolper, E. M. (1998).
730 Calculation of Peridotite Partial Melting from Thermodynamic Models of Minerals and
731 Melts. I. Review of Methods and Comparison with Experiments. *Journal of Petrology*. **39**,
732 1091–1115.

733 Hirschmann, M. M., Salters, V. & Blundy, J. (2000). Mantle solidus: Experimental constraints
734 and the effects of peridotite composition. *Geochemistry, Geophysics, Geosystems*. **1**.

735 Holloway, J. R., Pan, V. & Gudmundsson, G. (1992). High-pressure fluid absent melting
736 experiments in the presence of graphite: oxygen fugacity, ferric/ferrous ratio and dissolved
737 CO2. *European Journal of Mineralogy*. **4**, 105-114

738 Jakobsson, S. & Holloway, J. R. (2008). Mantle melting in equilibrium with an Iron-Wüstite-
739 Graphite buffered COH-fluid. *Contributions to Mineralogy and Petrology*. **155**, 247–256.

740 Kamenetsky, V. S., Pompilio, M., Métrich, N., Sobolev, A. V., Kuzmin, D. V. & Thomas, R.
741 (2007). Arrival of extremely volatile-rich high-Mg magmas changes explosivity of Mount
742 Etna. *Geology*. **35**, 255–258.

743 Kamenetsky, V. & Clocchiatti, R. (1996). Primitive magmatism of Mt. Etna: insights from
744 mineralogy and melt inclusions. *Earth and Planetary Science Letters*. **142**, 553–572.

745 Kawamoto, T., Yoshikawa, M., Kumagai, Y., Mirabueno, M. H. T., Okuno, M. & Kobayashi, T.
746 (2013). Mantle wedge infiltrated with saline fluids from dehydration and decarbonation of
747 subducting slab. *Proceedings of the National Academy of Sciences of the United States of*
748 *America* **110**, 9663–9668.

749 Kelemen, P. B. & Manning, C. E. (2015). Reevaluating carbon fluxes in subduction zones, what
750 goes down, mostly comes up. *Proceedings of the National Academy of Sciences of the*
751 *United States of America* **112**, 2020.

752 Kelemen, P. B. & Manning, C. E. (2022). Listvenite formation during mass transfer into the
753 leading edge of the mantle wedge: initial results from Oman drilling project hole BT1B.
754 *Journal of Geophysical Research: Solid Earth* 127, e2021JB022352.

755 Kelley, K. A. & Cottrell, E. (2009). Water and the oxidation state of subduction zone magmas.
756 *Science* **325**, 605–607.

757 Kerrick, D. M. & Connolly, J. A. D. (1998). Subduction of ophicarbonates and recycling of CO_2
758 and H_2O. *Geology*. **26**, 375–378.

759 Kerrick, D. M. & Connelly, J. A. D. (2001a). Metamorphic devolatilization of subducted marine
760 sediments and the transport of volatiles into the Earth's mantle. *Nature*. Nature Publishing
761 Group **411**, 293–296.

762 Kerrick, D. M. & Connelly, J. A. D. (2001b). Metamorphic devolatilization of subducted marine
763 oceanic metabasalts: implications for seismicity, arc magmatism and volatile recycling.
764 *Earth and Planetary Science Letters*. **189**, 19-29.

765 Kinzler, R. J. & Grove, T. L. (1992). Primary Magmas of Mid-Ocean Ridge Basalts 1.
766 Experiments and Methods. *JOURNAL OF GEOPHYSICAL RESEARCH* **97**, 6885–6906.

767 Kogiso, T. & Hirschmann, M. M. (2001). Experimental study of clinopyroxenite partial melting
768 and the origin of ultra-calcic melt inclusions. *Contributions to Mineralogy and Petrology*.
769 **142**, 347–360.

770 Kushiro, I. (1975). Carbonate-silicate reactions at high pressures and possible presence of
771 dolomite and magnesite in the upper mantle. *Earth and Planetary Science Letters* **28**, 116–
772 120.

773 Laporte, D., Toplis, M. J., Seyler, M. & Devidal, J. L. (2004). A new experimental technique for
774 extracting liquids from peridotite at very low degrees of melting: Application to partial
775 melting of depleted peridotite. *Contributions to Mineralogy and Petrology*. **146**, 463–484.

776 Lara, M. & Dasgupta, R. (2022). Carbon recycling efficiency in subduction zones constrained by
777 the effects of H_2O-CO_2 fluids on partial melt compositions in the mantle wedge. *Earth and*
778 *Planetary Science Letters*. **588**, 117578.

779 Lara, M. & Dasgupta, R. (2020). Partial melting of a depleted peridotite metasomatized by a
780 MORB-derived hydrous silicate melt – Implications for subduction zone magmatism.
781 *Geochimica et Cosmochimica Acta*. **290**, 137–161.

782 Lesher, C. E. & Walker, D. (1988). *Cumulate Maturation and Melt Migration in a Temperature*
783 *Gradient*. *Journal of Geophysical Research*. **93**, 10295-10311

784 Li, Y. (2017). Immiscible C-H-O fluids formed at subduction zone conditions. *Geochemical*
785 *Perspectives Letters* **3**, 12–21.

786 Litasov, K. D., Shatskiy, A. & Ohtani, E. (2014). Melting and subsolidus phase relations in
787 peridotite and eclogite systems with reduced COH fluid at 3-16 GPa. *Earth and Planetary*
788 *Science Letters*. **391**, 87–99.

789 Liu, S.-A., Wu, T., Li, S., Wang, Z. & Liu, J. (2022). Contrasting fates of subducting carbon
790 related to different oceanic slabs in East Asia. *Geochimica et Cosmochimica Acta* **324**, 156–
791 173.

792 Liu, Z., Rohrbach, A., Tiraboschi, C., Foley, S. F., Berndt, J. & Klemme, S. (2023). The effect of
793 COH fluids on partial melting of eclogite and lherzolite under moderately oxidizing and
794 reducing conditions. *Chemical Geology*. **616**, 121219.

795 Mallik, A. & Dasgupta, R. (2013). Reactive Infiltration of MORB-Eclogite-Derived Carbonated
796 Silicate Melt into Fertile Peridotite at 3 GPa and Genesis of Alkalic Magmas. *Journal of*
797 *Petrology* **54**, 2267–2300.

798 Mallik, A., Dasgupta, R., Tsuno, K. & Nelson, J. (2016). Effects of water, depth and temperature
799 on partial melting of mantle-wedge fluxed by hydrous sediment-melt in subduction zones.
800 *Geochimica et Cosmochimica Acta* **195**, 226–243.

801 Mallik, A., Nelson, J. & Dasgupta, R. (2015). Partial melting of fertile peridotite fluxed by
802 hydrous rhyolitic melt at 2–3 GPa: implications for mantle wedge hybridization by sediment
803 melt and generation of ultrapotassic magmas in convergent margins. *Contributions to*
804 *Mineralogy and Petrology*. **169**, 48.

805 Mandler, B. E. & Grove, T. L. (2016). Controls on the stability and composition of amphibole in
806 the Earth's mantle. *Contributions to Mineralogy and Petrology*. **171**, 68.

Martin, L. A. J. & Hermann, J. (2018). Experimental phase relations in altered oceanic crust: Implications for carbon recycling at subduction zones. *Journal of Petrology*. **59**, 299–320.

Médard, E., Schmidt, M. W., Schiano, P. & Ottolini, L. (2006). Melting of Amphibole-bearing Wehrlites: an Experimental Study on the Origin of Ultra-calcic Nepheline-normative Melts. *Journal of Petrology*. **47**, 481–504.

Menzel, M. D., Garrido, C. J. & López Sánchez-Vizcaíno, V. (2020). Fluid-mediated carbon release from serpentinite-hosted carbonates during dehydration of antigorite-serpentinite in subduction zones. *Earth and Planetary Science Letters*. **531**, 115964.

Mitchell, A. L. & Grove, T. L. (2015). Melting the hydrous, subarc mantle: the origin of primitive andesites. *Contributions to Mineralogy and Petrology*. **170**, 13.

Molina, J. F. & Poli, S. (2000). Carbonate stability and fluid composition in subducted oceanic crust: An experimental study on H2O-CO2-bearing basalts. *Earth and Planetary Science Letters* **176**, 295–310.

Mysen, B. R. O. & Boettcher, A. L. (1975). Melting of a Hydrous Mantle: I. Phase Relations of Natural Peridotite at High Pressures and Temperatures with Controlled Activities of Water, Carbon Dioxide, and Hydrogen. *Journal of Petrology*. **16**, 520–548.

Pearce, J. A., Kempton, P. D. & Gill, J. B. (2007). Hf-Nd evidence for the origin and distribution of mantle domains in the SW Pacific. *Earth and Planetary Science Letters* **260**, 98–114.

Perrin, A., Goes, S., Prytulak, J., Rondenay, S. & Davies, D. R. (2018). Mantle wedge temperatures and their potential relation to volcanic arc location. *Earth and Planetary Science Letters*. **501**, 67–77.

Pintér, Z., Foley, S. F., Yaxley, G. M., Rosenthal, A., Rapp, R. P., Lanati, A. W. & Rushmer, T. (2021). Experimental investigation of the composition of incipient melts in upper mantle peridotites in the presence of CO2 and H2O. *Lithos*. **396**–**397**, 106224.

Pirard, C. & Hermann, J. (2015). Focused fluid transfer through the mantle above subduction zones. *Geology*. **43**, 915–918.

Plank, T. & Langmuir, C. H. (1988). An evaluation of the global variations in the major element chemistry of arc basalts. *Earth and Planetary Science Letters*. **90**, 349–370.

Rapp, R. ., Shimizu, N., Norman, M. . & Applegate, G. . (1999). Reaction between slab-derived melts and peridotite in the mantle wedge: experimental constraints at 3.8 GPa. *Chemical Geology*. **160**, 335–356.

Roeder, P. L. & Emslie, R. F. (1970). Olivine-liquid equilibrium. *Contributions to Mineralogy and Petrology*. **29**, 275–289.

Saha, S. & Dasgupta, R. (2019). Phase Relations of a Depleted Peridotite Fluxed by a CO_2-H_2O Fluid—Implications for the Stability of Partial Melts Versus Volatile-Bearing Mineral Phases in the Cratonic Mantle. *Journal of Geophysical Research: Solid Earth*. **124**, 10089–10106.

Sapienza, G. T., Marco, A. E., Ae, S., Braga, R. & Scambelluri, M. (2009). Dolomite-bearing orogenic garnet peridotites witness fluid-mediated carbon recycling in a mantle wedge (Ulten Zone, Eastern Alps, Italy). *Contributions to Mineralogy and Petrology* **158**, 401–420.

Schiano, P., Eiler, J. M., Hutcheon, I. D. & Stolper, E. M. (2000). Primitive CaO-rich, silica-undersaturated melts in island arcs: Evidence for the involvement of clinopyroxene-rich lithologies in the petrogenesis of arc magmas. *Geochemistry, Geophysics, Geosystems*. **1**.

Schmidt, M. W. & Jagoutz, O. (2017). The global systematics of primitive arc melts. *Geochemistry, Geophysics, Geosystems*. **18**, 2817–2854.

Schwab, B. E. & Johnston, A. D. (2001). Melting Systematics of Modally Variable, Compositionally Intermediate Peridotites and the Effects of Mineral Fertility. *Journal of Petrology*. **42**, 1789–1811.

Song, S., Su, L., Niu, Y., Lai, Y. & Zhang, L. (2009). CH_4 inclusions in orogenic harzburgite: Evidence for reduced slab fluids and implication for redox melting in mantle wedge. *Geochimica et Cosmochimica Acta*. **73**, 1737–1754.

Sorbadere, F., Schiano, P. & Métrich, N. (2013). Constraints on the Origin of Nepheline-Normative Primitive Magmas in Island Arcs Inferred from Olivine-hosted Melt Inclusion Compositions. *Journal of Petrology*. **54**, 215–233.

Sorbadere, F., Schiano, P., Métrich, N. & Garaebiti, E. (2011). Insights into the origin of primitive silica-undersaturated arc magmas of Aoba volcano (Vanuatu arc). *Contributions to Mineralogy and Petrology*. **162**, 995–1009.

Spandler, C. & Pirard, C. (2013). Element recycling from subducting slabs to arc crust: A review. *Lithos*. **170**–**171**, 208–223.

Stagno, V., Ojwang, D. O., McCammon, C. A. & Frost, D. J. (2013). The oxidation state of the mantle and the extraction of carbon from Earth's interior. *Nature*. Nature Publishing Group **493**, 84–88.

Sun, C. & Dasgupta, R. (2019). Slab–mantle interaction, carbon transport, and kimberlite generation in the deep upper mantle. *Earth and Planetary Science Letters*. **506**, 38–52.

Syracuse, E. M., van Keken, P. E. & Abers, G. A. (2010). The global range of subduction zone thermal models. *Physics of the Earth and Planetary Interiors*. **183**, 73–90.

874 Tenner, T. J., Hirschmann, M. M. & Humayun, M. (2012). The effect of H_2O on partial melting
875 of garnet peridotite at 3.5 GPa. *Geochemistry, Geophysics, Geosystems*. **13**.

876 Thomsen, T. B. & Schmidt, M. W. (2008). Melting of carbonated pelites at 2.5-5.0 GPa, silicate-
877 carbonatite liquid immiscibility, and potassium-carbon metasomatism of the mantle. *Earth*
878 *and Planetary Science Letters* **267**, 17–31.

879 Thomson, A. R., Walter, M. J., Kohn, S. C. & Brooker, R. A. (2016). Slab melting as a barrier to
880 deep carbon subduction. *Nature*. **529**, 76–79.

881 Till, C. B., Grove, T. L. & Withers, A. C. (2012). The beginnings of hydrous mantle wedge
882 melting. *Contributions to Mineralogy and Petrology*. **163**, 669–688.

883 Tollstrup, D., Gill, J., Kent, A., Prinkey, D., Williams, R., Tamura, Y. & Ishizuka, O. (2010).
884 Across-arc geochemical trends in the Izu-Bonin arc: Contributions from the subducting
885 slab, revisited. *Geochemistry, Geophysics, Geosystems*. **11**.

886 Toplis, M. J. (2005). The thermodynamics of iron and magnesium partitioning between olivine
887 and liquid: Criteria for assessing and predicting equilibrium in natural and experimental
888 systems. *Contributions to Mineralogy and Petrology*. **149**, 22–39.

889 Tsuno, K. & Dasgupta, R. (2011). Melting phase relation of nominally anhydrous, carbonated
890 pelitic-eclogite at 2.5–3.0 GPa and deep cycling of sedimentary carbon. *Contributions to*
891 *Mineralogy and Petrology*. **161**, 743–763.

892 Tsuno, K. & Dasgupta, R. (2012). The effect of carbonates on near-solidus melting of pelite at 3
893 GPa: Relative efficiently of H_2O and CO_2 subduction. *Earth and Planetary Science Letters*.
894 **319-320**, 185-196.

895 Tumiati, S., Tiraboschi, C., Sverjensky, D. A., Pettke, T., Recchia, S., Ulmer, P., Miozzi, F. &
896 Poli, & S. (2017) Silicate dissolution boosts the CO_2 concentrations in subduction fluids.
897 *Nature Communications*. **8**, 616

898 Tumiati, S., Recchia, S., Remusat, L., Tiraboschi, C., Sverjensky, D. A., Manning, C.E., Vitale
899 Brovarone, A., Boutier, A., Spanu, D., Poli, S. (2022). Subducted organic matter buffered
900 by marine carbonate rules the carbon isotopic signature of arc emissions. *Nature*
901 *Communications.* **13**, 1–10.

902 Turner, S. J. & Langmuir, C. H. (2022). An evaluation of five models of arc volcanism. *Journal*
903 *of Petrology*. **63**, 1-25

904 Turner, S. J. & Langmuir, C. H. (2015). What processes control the chemical compositions of arc
905 front stratovolcanoes? *Geochemistry, Geophysics, Geosystems*. **16**, 1865–1893.

906 Turner, S. J. & Langmuir, C. H. (2022). A quantitative framework for global variations in arc
907 geochemistry. *Earth and Planetary Science Letters* **584**, 117411.

Turner, S. J., Langmuir, C. H., Dungan, M. A. & Escrig, S. (2017). The importance of mantle wedge heterogeneity to subduction zone magmatism and the origin of EM1. *Earth and Planetary Science Letters*. **472**, 216–228.

Turner, S. J., Langmuir, C. H., Katz, R. F., Dungan, M. A. & Escrig, S. (2016). Parental arc magma compositions dominantly controlled by mantle-wedge thermal structure. *Nature Geoscience*. **9**, 772–776.

Ulmer, P. (2001). Partial melting in the mantle wedge — the role of H_2O in the genesis of mantle-derived 'arc-related' magmas. *Physics of the Earth and Planetary Interiors*. **127**, 215–232.

Wallace, M. E. & Green, D. H. (1988). An experimental determination of primary carbonatite magma composition. *Nature*. **335**, 343–346.

Wallace, P. J. (2005). Volatiles in subduction zone magmas: Concentrations and fluxes based on melt inclusion and volcanic gas data. *Journal of Volcanology and Geothermal Research*. **140**, 217–240.

Wasylenki, L. E., Baker, M. B., Kent, A. J. R. & Stolper, E. M. (2003). Near-solidus Melting of the Shallow Upper Mantle: Partial Melting Experiments on Depleted Peridotite. *Journal of Petrology*. **44**, 1163–1191.

Woodhead, J., Stern, R. J., Pearce, J., Hergt, J. & Vervoort, J. (2012). Hf-Nd isotope variation in Mariana Trough basalts: The importance of "ambient mantle" in the interpretation of subduction zone magmas. *Geology*. **40**, 539–542.

Yoder, H.S., Tilley, C.E. (1962). Origin of Basalt Magmas: An Experimental Study of Natural and Synthetic Rock Systems. *Journal of Petrology*. **3**, 342-532

Figure 1. (A) CaO and Al_2O_3 compositions of peridotite xenoliths from convergent margins (Andean, High Cascades, Honshu, Kamchatka, Kurlile, Mariana, Sikhote-Alin-Sakhalin, Sulawesi) downloaded from georoc (February 27, 2022). Decreasing CaO and Al_2O_3 coupled with increasing Mg# reflect the varying extents of melt depletion in mantle wedge peridotites. The orange square and purple diamond are the fertile and depleted peridotite compositions used in this study, respectively. (B) Gray field is the pressure-temperature domain of melt generation in mantle wedges bounded by the C-O-H fluid saturated solidus (Falloon & Green, 1990; Dvir & Kessel, 2017) and the global range of maximum mantle wedge temperatures (small black dots) from Syracuse et al. (2010). Blue squares are the experimental *P-T* conditions from Lara & Dasgupta (2022). Red squares are the *P-T* conditions explored in this study.

Figure 2. SiO_2 and CaO concentrations of experimental partial melts generated at 1.0-3.5 GPa plotted on a volatile free basis using dry peridotite (Hirose & Kushiro, 1993, Laporte et al., 2004), peridotite + CO_2 (Dasgupta et al., 2007) peridotite + H_2O (Tenner et al., 2012; Pirard & Hermann, 2015; Mallik et al., 2015, 2016; Grove & Till, 2019; Lara & Dasgupta, 2020) and peridotite + H_2O + CO_2 compositions (Lara & Dasgupta, 2022) plotted against the extent of melting of each experiment. Each data point for volatile-bearing experiments is filled according to the colorbar, which represents the XCO_2 of the bulk compositions in each experiment. Light grey bands are the spread of SiO_2 and CaO concentrations observed in primitive arc magmas from Schmidt & Jagoutz (2017). Note that the SiO_2 and CaO compositions of partial melts from peridotite + H_2O vs. peridotite + CO_2 systems diverge as the solidus is approached, while the SiO_2 and CaO concentrations of dry peridotite partial melts remain relatively constant throughout the entire melting interval.

Figure 3. Typical BSE images of experiments performed in this study at 2-3 GPa and 1350 °C. All experiments consisted of olivine + opx + melt. (A) Full capsule BSE image of experiment

B516 performed using the depleted peridotite composition at 2 GPa with XCO_2 = 0.04. (B) Magnified BSE image of quenched melt texture consisting of a homogeneous distribution of metastable quench crystals corresponding to the red box in Figure 3A. (C) Full capsule BSE image of experiment B505 performed using the depleted peridotite composition at 2 GPa with XCO_2 = 0.11. (D) Magnified BSE image of quenched melt texture consisting of a more heterogeneous distribution of metastable quench crystals corresponding to the red box in Figure 3C. (E) Full capsule BSE image of experiment B515 performed using the fertile peridotite composition at 3 GPa with XCO_2 = 0.17. (F) Magnified BSE image of quenched melt texture consisting of glassy patches corresponding to the red box in Figure 3E.

Figure 4. Major element compositions of Fe-corrected experimental partial melts produced in this study plotted on a volatile-free basis and as a function of bulk XCO_2 [= molar $CO_2/(CO_2+H_2O)$]. All melts were generated at a constant temperature of 1350 °C and ±1σ error bars are based on replicate electron microprobe analyses. Note that even at a constant *P*-*T*, XCO_2 and peridotite fertility have large effects on nearly all major oxides of experimental partial melts.

Figure 5. 2 GPa melt compositions from depleted peridotite experiments at 1350 °C in this study (red circles) compared to identical depleted peridotite experiments from Lara & Dasgupta (2022) -LD22 at 1200°C (blue circles) plotted as a function of the nominal XCO_2 of bulk composition. All melts are plotted on a volatile-free basis. Vertical error bars on data are ±1σ uncertainties based on replicate microprobe analyses, as given in Table 5 and reported in Lara & Dasgupta (2022).

Figure 6. 3 GPa melt compositions from depleted peridotite experiments at 1350 °C in this study (red squares) compared to identical depleted peridotite experiments from Lara & Dasgupta (2022)-LD22 at 1200°C (blue squares) plotted as a function of the nominal XCO_2 of bulk composition. All melts are plotted on a volatile-free basis. Vertical error bars on data are ±1σ uncertainties based on replicate microprobe analyses, as given in Table 5 and reported in Lara & Dasgupta (2022).

Figure 7. (A) The extent of melting in experiments from this study calculated by mass balance and plotted as a function of nominal XCO_2 of bulk composition. Error in extent of melting is smaller than the data points. Note that the extent of melting increases at a constant temperature as XCO_2 decreases and peridotite fertility increases. (B) The extent of melting plotted as a function of temperature from this study, the depleted peridotite + H_2O + CO_2 study of Lara & Dasgupta (2022), and the depleted and fertile peridotite + H_2O studies of Lara & Dasgupta (2020) and Grove & Till (2019), respectively. Data points are filled according to the legend which illustrates the XCO_2 of the experiment plotted with black data points representing nominally CO_2-free, hydrous peridotite experiments. Note that isobaric melt productivities typically increase as XCO_2 decreases and fertility increases. (C) Mineral and melt modes in depleted peridotite + H_2O experiments at 3 GPa from 1050 °C to 1250 °C from the experiments of Lara & Dasgupta (2020) in 7B. (D) Mineral and melt modes in fertile peridotite + H_2O experiments at 3.2 GPa from 1075 °C to 1150 °C from the experiments of Grove & Till (2019) in 7B. Ol – olivine, Opx – orthopyroxene, CPX – clinopyroxene, Gnt – garnet.

Figure 8. Solidi locations of H_2O-fluid saturated peridotite from Grove et al. (2006)-G06, Till et al. (2012)-T12 and Green (1973)-G73, H_2O-CO_2 fluid-saturated peridotite from Falloon & Green (1990)-FG90 and Wallace & Green (1988)-WG88, carbonated peridotite from Falloon & Green (1989)-FG89 and dry peridotite from Hirschmann (2000)-H00. Note that near 2 GPa, the solidus temperature of peridotite increases as bulk XCO_2 increases.

Figure 9. Major element compositions of experimental partial melts plotted on a volatile-free basis from this study (right panel), the high pressure depleted and fertile peridotite + H_2O studies of Lara & Dasgupta (2020), Grove & Till (2019) and Mitchell & Grove (2015) (left panel) all plotted as a function of extent of melting. Each data point is filled according to the XCO_2 of the starting compositions with black data points representing CO_2-free hydrous peridotite experiments. Black lines connect fertile and depleted peridotite experiments run at near identical P-T. Vertical error bars on data are ±1σ uncertainties based on replicate microprobe analyses, as given in Table 5.

Figure 10. Major element compositions of fertile peridotite experimental partial melts plotted on volatile free bases as a function of extent of melting. The data are separated into partial melts derived from oxidized peridotite + H_2O + CO_2 experiments and reduced peridotite + H_2O + CH_4 experiments as indicated by the color bars, which represent the XCO_2 or XCH_4 of the starting compositions from which the partial melts are derived. The gray field represents the compositional space of partial melts from fertile peridotite + H_2O experiments compiled from the studies by Grove & Till (2019), Tenner et al., (2012), Mitchell & Grove (2015), and Pirard & Hermann (2015). Vertical error bars on data are ±1σ uncertainties based on replicate microprobe analyses, as given in Table 5.

Figure 11. SiO_2/CaO weight ratios vs MgO of fractionation corrected experimental partial melts from this study, the depleted peridotite + H_2O + CO_2 study of Lara & Dasgupta (2022), the depleted peridotite + H_2O study of Lara & Dasgupta (2020) and the fertile peridotite + H_2O studies of Tenner et al. (2013) and Grove & Till (2019). All experimental melts are plotted on a volatile-free basis and compared to primitive arc melts from Schmidt & Jagoutz (2017) and ultra-calcic melt inclusions (Kamenetsky & Clocchiatii, 1996; Schiano, 2000; Kamenestsky et al., 2007; Elburg et al., 2007; Sorbadere et al., 2011). Data points are filled according to the legend which illustrates the XCO_2 of the experiment plotted. Vertical error bars on experimental melts from this study are ±1σ uncertainties based on replicate microprobe analyses, as given in Table 5. Note that all bulk compositions with $XCO_2 > 0.04$ from 1200 – 1350 °C produce melts with lower SiO_2/CaO than all primitive arc melts.

Figure 12. CaO/Al_2O_3 ratios of fractionation corrected experimental melts as shown in Figure 10 plotted as a function of MgO content. All experimental melts are plotted on a volatile-free basis and compared to ultra-calcic melt inclusions (Kamenetsky & Clocchiatii, 1996; Schiano, 2000; Kamenestsky et al., 2007; Elburg et al., 2007; Sorbadere et al., 2011). Grey field is the CaO/Al_2O_3 – MgO space covered by the global range of primitive arc melts (PAM) from Schmidt & Jagoutz (2017). Data points are filled according to the legend which illustrates the XCO_2 of the experiment plotted. Vertical error bars on data are ±1σ uncertainties based on replicate microprobe analyses, as given in Table 5.

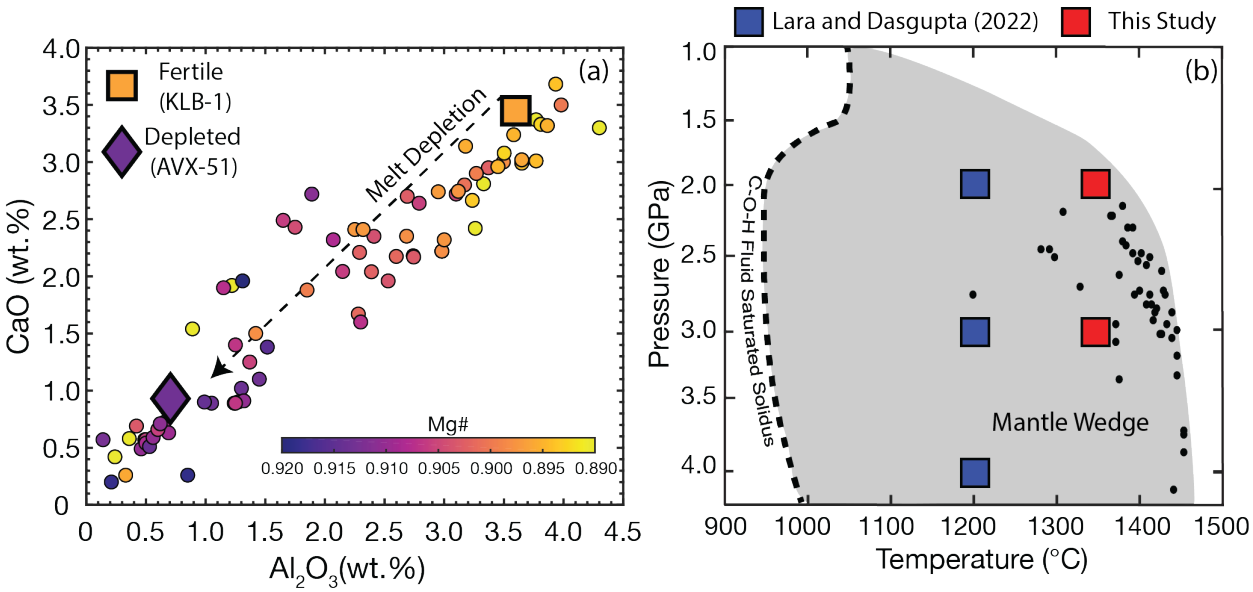

Figure 1. (A) CaO and Al_2O_3 compositions of peridotite xenoliths from convergent margins (Andean, High Cascades, Honshu, Kamchatka, Kurlile, Mariana, Sikhote-Alin-Sakhalin, Sulawesi) downloaded from georoc (February 27, 2022). Decreasing CaO and Al_2O_3 coupled with increasing Mg# reflect the varying extents of melt depletion in mantle wedge peridotites. The orange square and purple diamond are the fertile and depleted peridotite compositions used in this study, respectively. (B) Gray field is the pressure-temperature domain of melt generation in mantle wedges bounded by the C-O-H fluid saturated solidus (Falloon and Green, 1990; Dvir and Kessel, 2017) and the global range of maximum mantle wedge temperatures (small black dots) from Syracuse et al. (2010). Blue squares are the experimental *P-T* conditions from Lara and Dasgupta (2022). Red squares are the *P-T* conditions explored in this study.

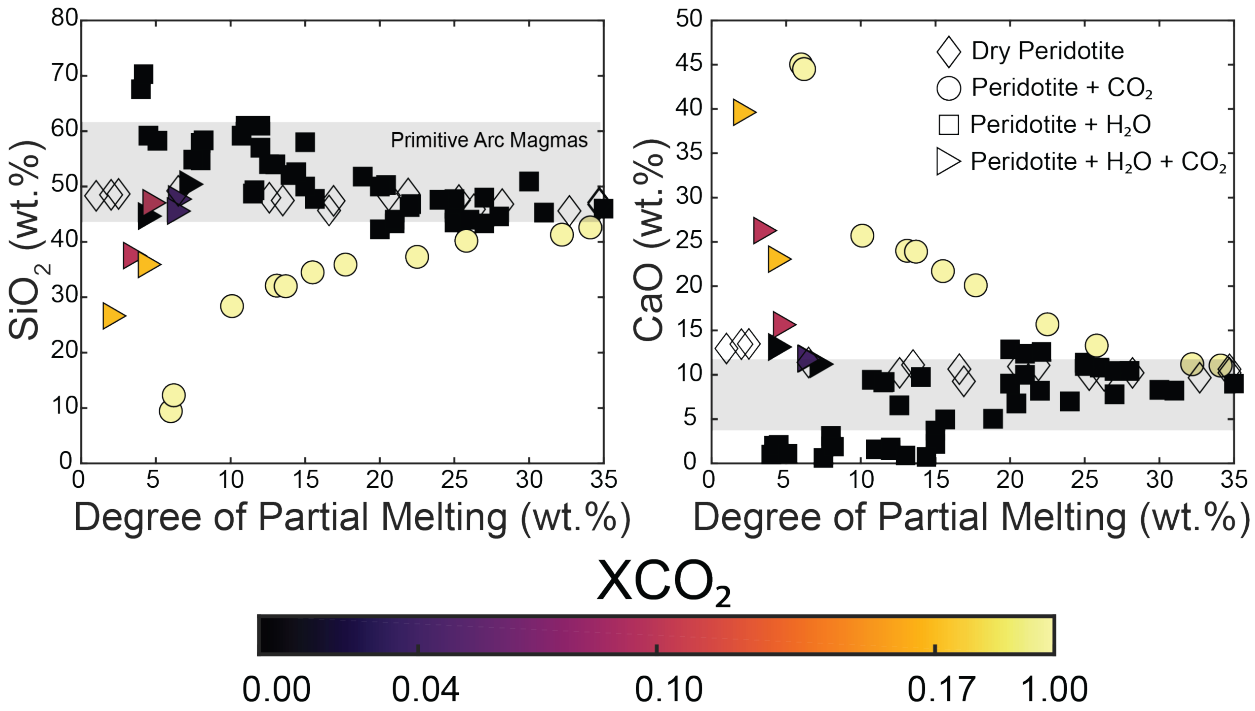

Figure 2. SiO_2 and CaO concentrations of experimental partial melts generated at 1.0-3.5 GPa plotted on a volatile free basis using dry peridotite (Hirose and Kushiro, 1993, Laporte et al., 2004), peridotite + CO_2 (Dasgupta et al., 2007) peridotite + H_2O (Tenner et al., 2012; Pirard and Hermann, 2015; Mallik et al., 2015, 2016; Grove and Till, 2019; Lara and Dasgupta, 2020) and peridotite + H_2O + CO_2 compositions (Lara and Dasgupta, 2022) plotted against the extent of melting of each experiment. Each data point for volatile-bearing experiments is filled according to the colorbar, which represents the XCO_2 of the bulk compositions in each experiment. Light grey bands are the spread of SiO_2 and CaO concentrations observed in primitive arc magmas from Schmidt and Jagoutz (2017). Note that the SiO_2 and CaO compositions of partial melts from peridotite + H_2O vs. peridotite + CO_2 systems diverge as the solidus is approached, while the SiO_2 and CaO concentrations of dry peridotite partial melts remain relatively constant throughout the entire melting interval.

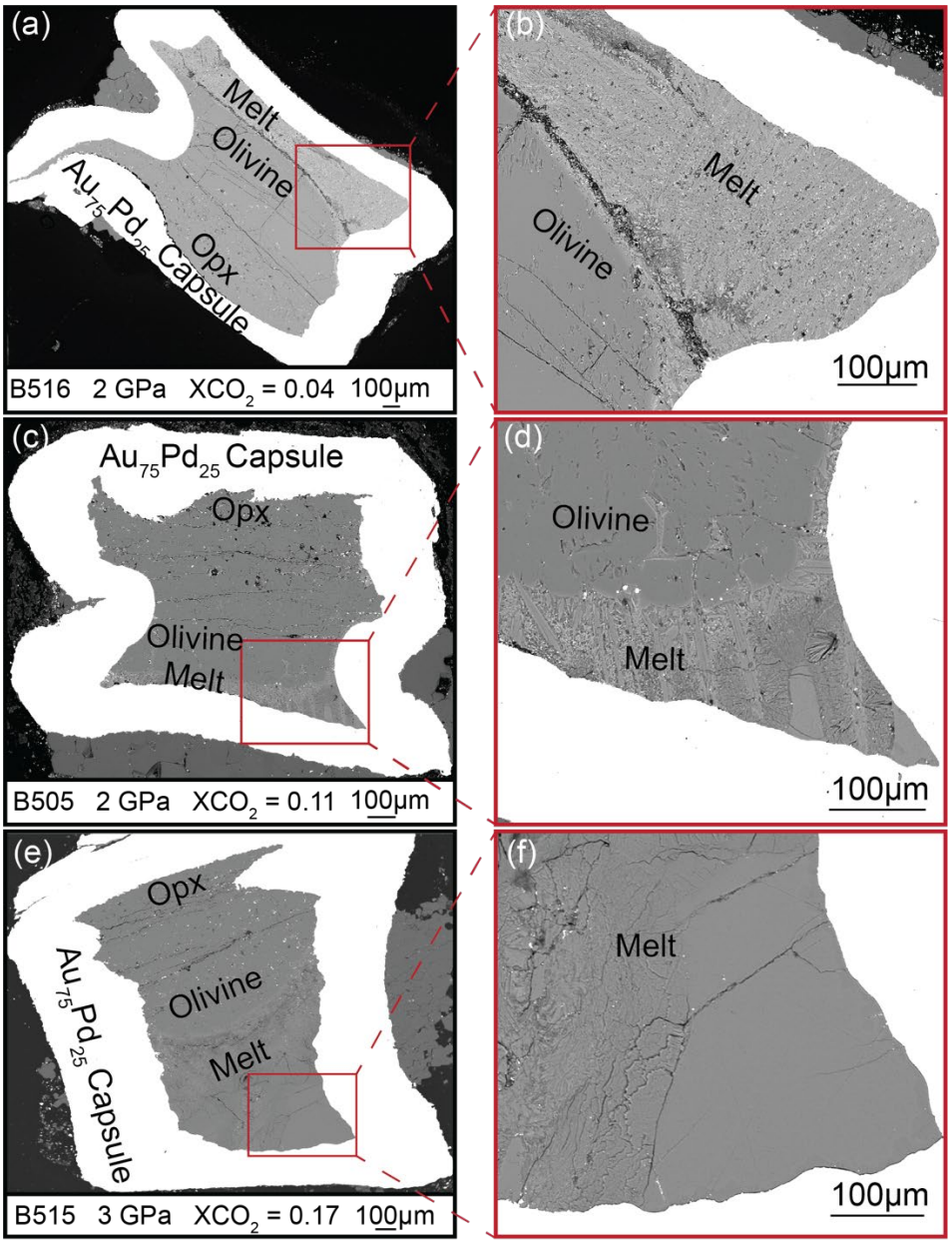

Figure 3. Typical BSE images of experiments performed in this study at 2-3 GPa and 1350 °C. All experiments consisted of olivine + opx + melt. (A) Full capsule BSE image of experiment B516 performed using the depleted peridotite composition at 2 GPa with $XCO_2 = 0.04$. (B) Magnified BSE image of quenched melt texture consisting of a homogeneous distribution of metastable quench crystals corresponding to the red box in Figure 3A. (C) Full capsule BSE image of experiment B505 performed using the depleted peridotite composition at 2 GPa with $XCO_2 = 0.11$. (D) Magnified BSE image of quenched melt texture consisting of a more heterogeneous distribution of metastable quench crystals corresponding to the red box in Figure 3C. (E) Full capsule BSE image of experiment B515 performed using the fertile peridotite composition at 3 GPa with $XCO_2 = 0.17$. (F) Magnified BSE image of quenched melt texture consisting of glassy patches corresponding to the red box in Figure 3E.

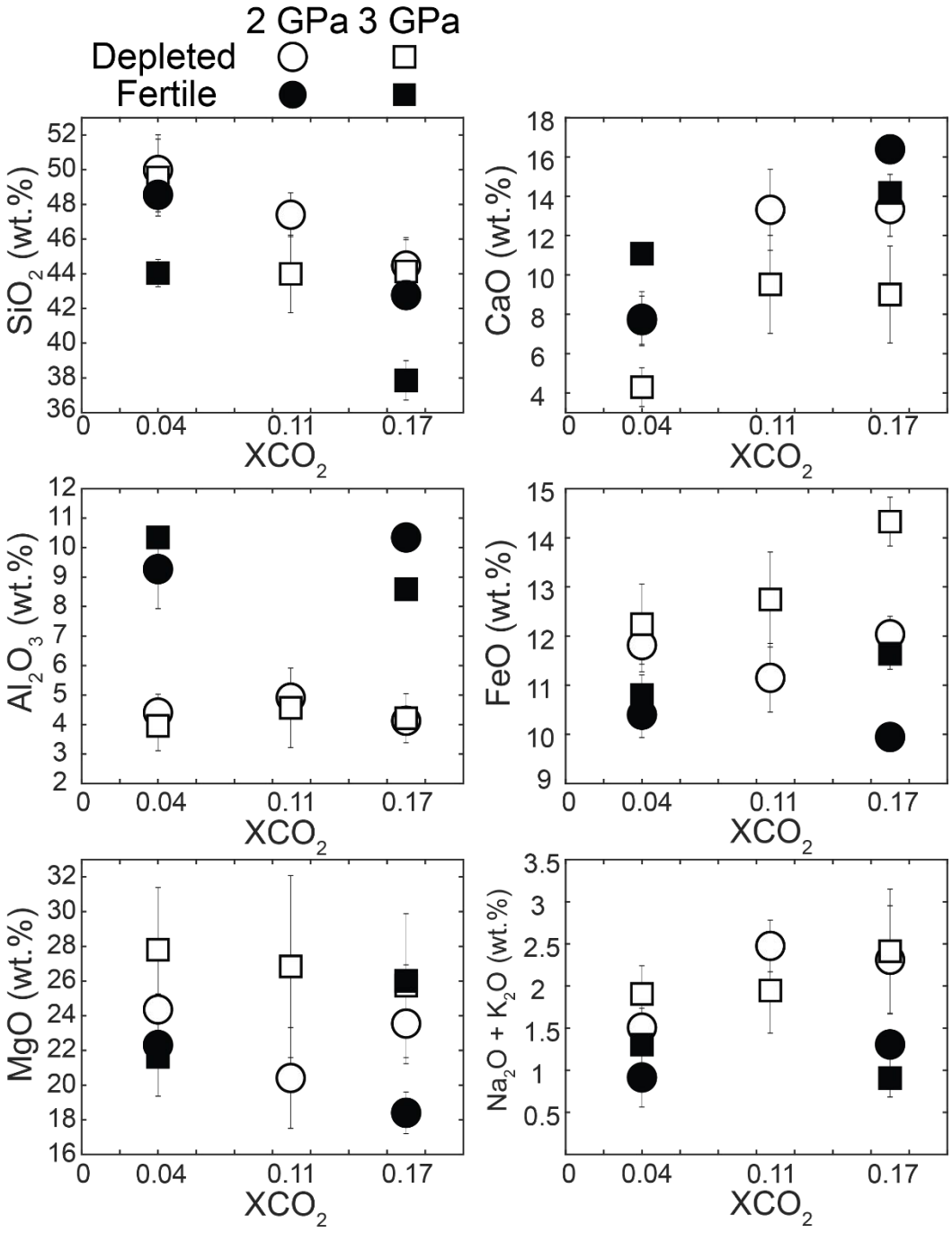

Figure 4. Major element compositions of Fe-corrected experimental partial melts produced in this study plotted on a volatile-free basis and as a function of bulk XCO_2 [= molar $CO_2/(CO_2+H_2O)$]. All melts were generated at a constant temperature of 1350 °C and ±1σ error bars are based on replicate electron microprobe analyses. Note that even at a constant *P*-*T*, XCO_2 and peridotite fertility have large effects on nearly all major oxides of experimental partial melts.

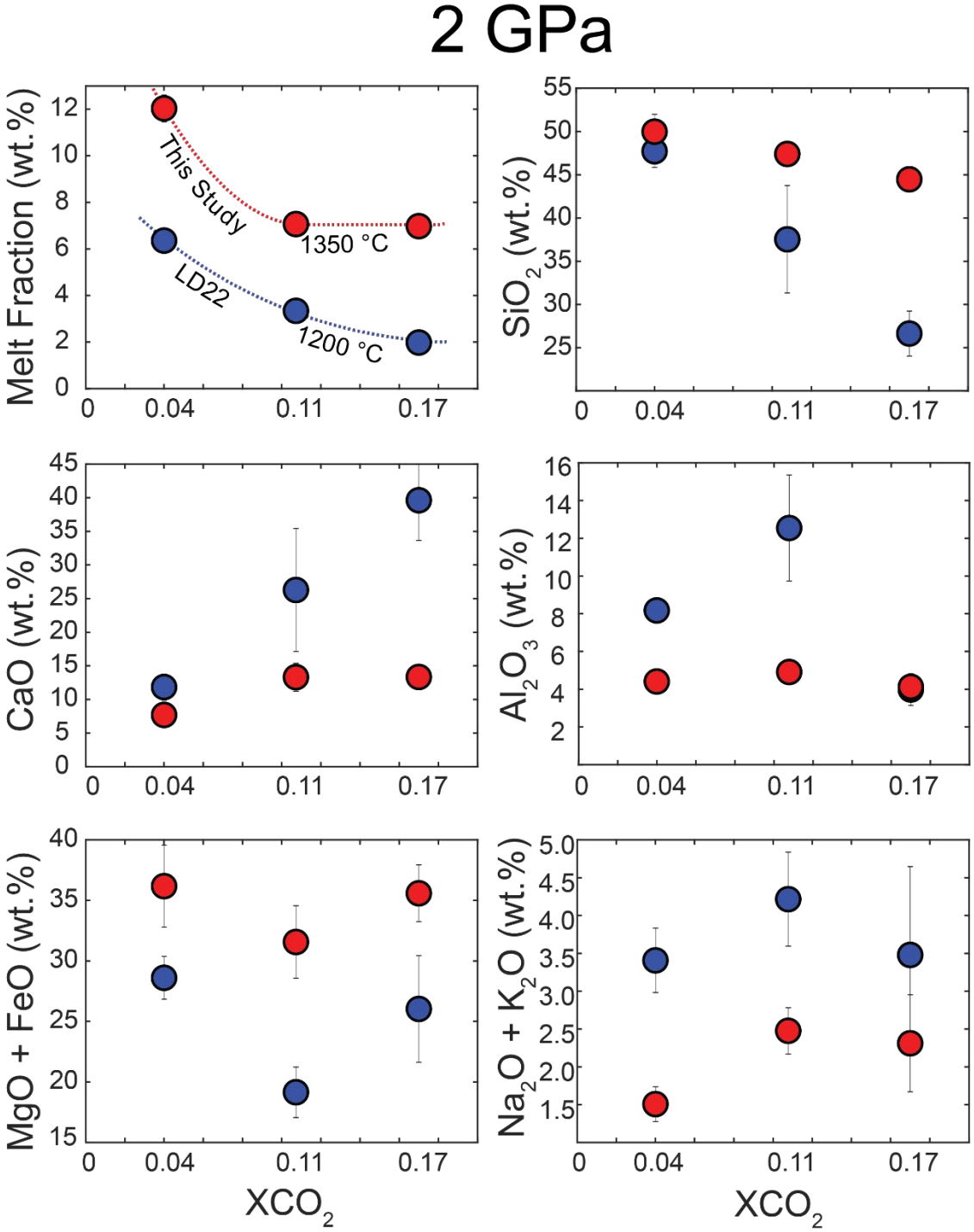

Figure 5. 2 GPa melt compositions from depleted peridotite experiments at 1350 °C in this study (red circles) compared to identical depleted peridotite experiments from Lara and Dasgupta (2022) at 1200 °C (blue circles) plotted as a function of the nominal XCO_2 of bulk composition. All melts are plotted on a volatile-free basis. Vertical error bars on data are ±1σ uncertainties based on replicate microprobe analyses, as given in Table 3 and reported in Lara and Dasgupta (2022).

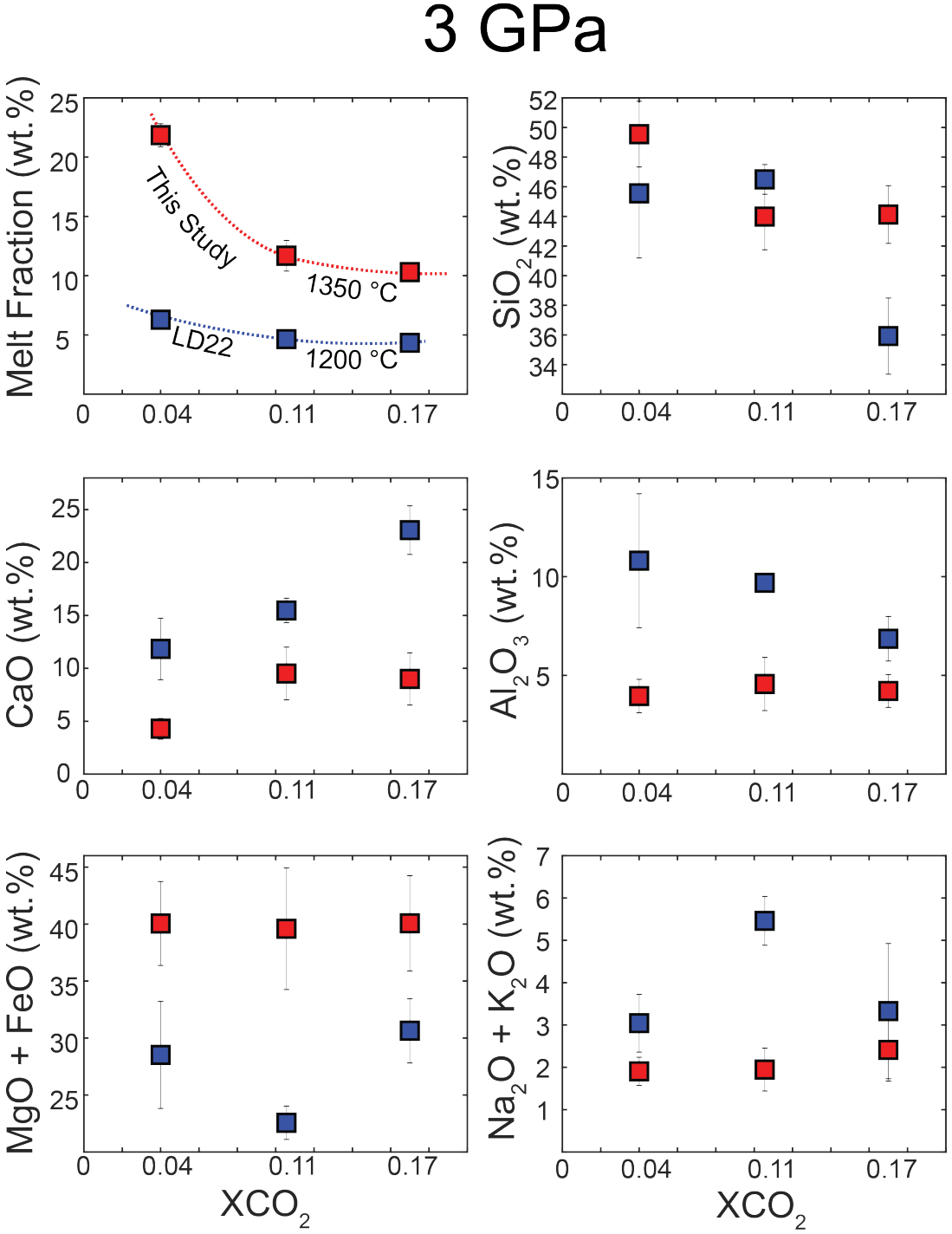

Figure 6. 3 GPa melt compositions from depleted peridotite experiments at 1350 °C in this study (red squares) compared to identical depleted peridotite experiments from Lara and Dasgupta (2022)-LD20 at 1200 °C (blue squares) plotted as a function of the nominal XCO_2 of bulk composition. All melts are plotted on a volatile-free basis. Vertical error bars on data are ±1σ uncertainties based on replicate microprobe analyses, as given in Table 3 and reported in Lara and Dasgupta (2022).

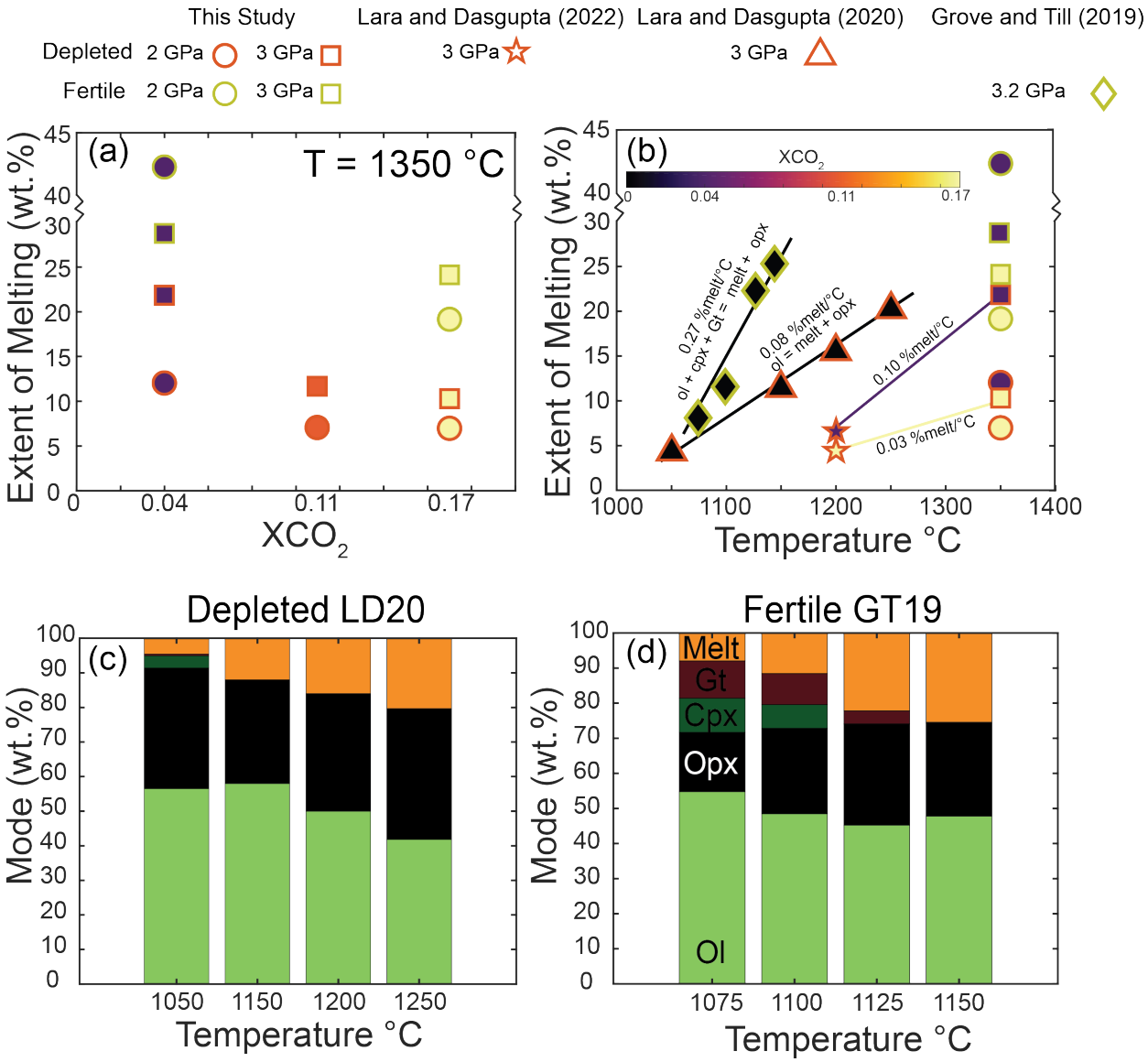

Figure 7. (A) The extent of melting in experiments from this study calculated by mass balance and plotted as a function of nominal XCO_2 of bulk composition. Error in extent of melting is smaller than the data points. Note that the extent of melting increases at a constant temperature as XCO_2 decreases and peridotite fertility increases. (B) The extent of melting plotted as a function of temperature from this study, the depleted peridotite + H_2O + CO_2 study of Lara and Dasgupta (2022), and the depleted and fertile peridotite + H_2O studies of Lara & Dasgupta (2020) and Grove & Till (2019), respectively. Each data point is filled according to the color bar with black data points representing nominally CO_2-free, hydrous peridotite experiments. Note that isobaric melt productivities typically increase as XCO_2 decreases and fertility increases. (C) Mineral and melt modes in depleted peridotite + H_2O experiments at 3 GPa from 1050 °C to 1250 °C from the experiments of Lara and Dasgupta (2020) in 7B. (D) Mineral and melt modes in fertile peridotite + H_2O experiments at 3.2 GPa from 1075 °C to 1150 °C from the experiments of Grove and Till (2019) in 7B.

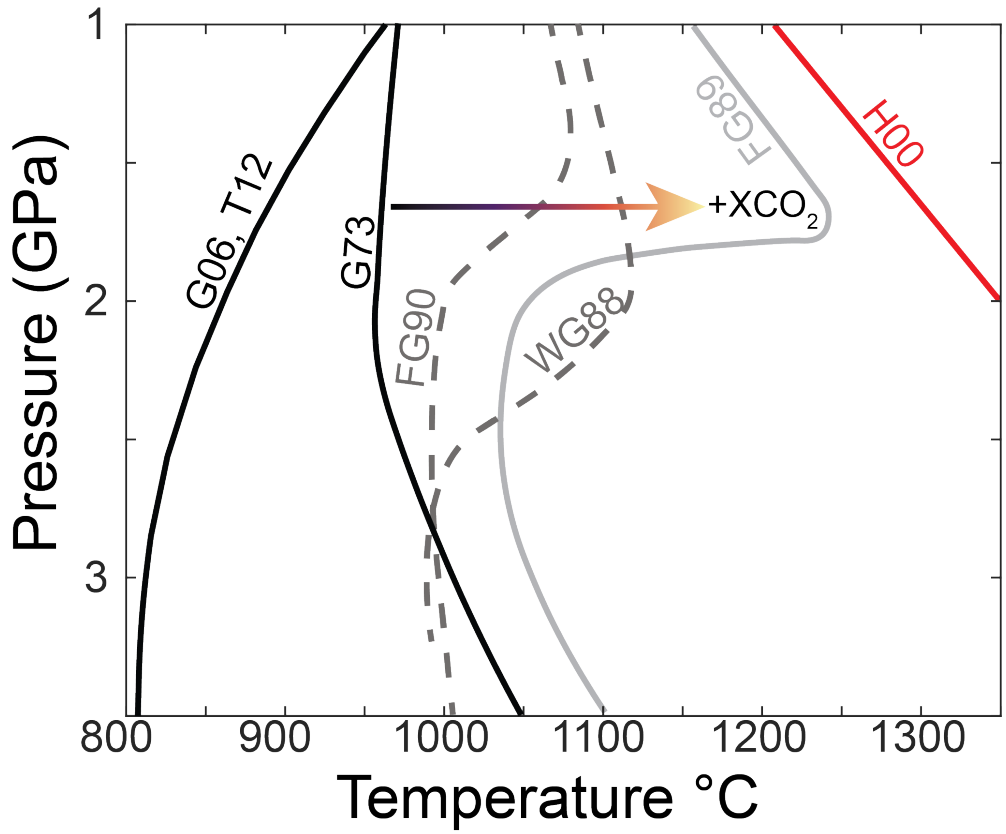

Figure 8. Solidi locations of H_2O-fluid saturated peridotite from Grove et al. (2006)-G06, Till et al. (2012)-T12 and Green (1973)-G73, H_2O-CO_2 fluid-saturated peridotite from Falloon and Green (1990)-FG90 and Wallace and Green (1988)-WG88, carbonated peridotite from Falloon and Green (1989)-FG89 and dry peridotite from Hirschmann (2000)-H00. Note that near 2 GPa, the solidus temperature of peridotite increases as bulk XCO_2 increases.

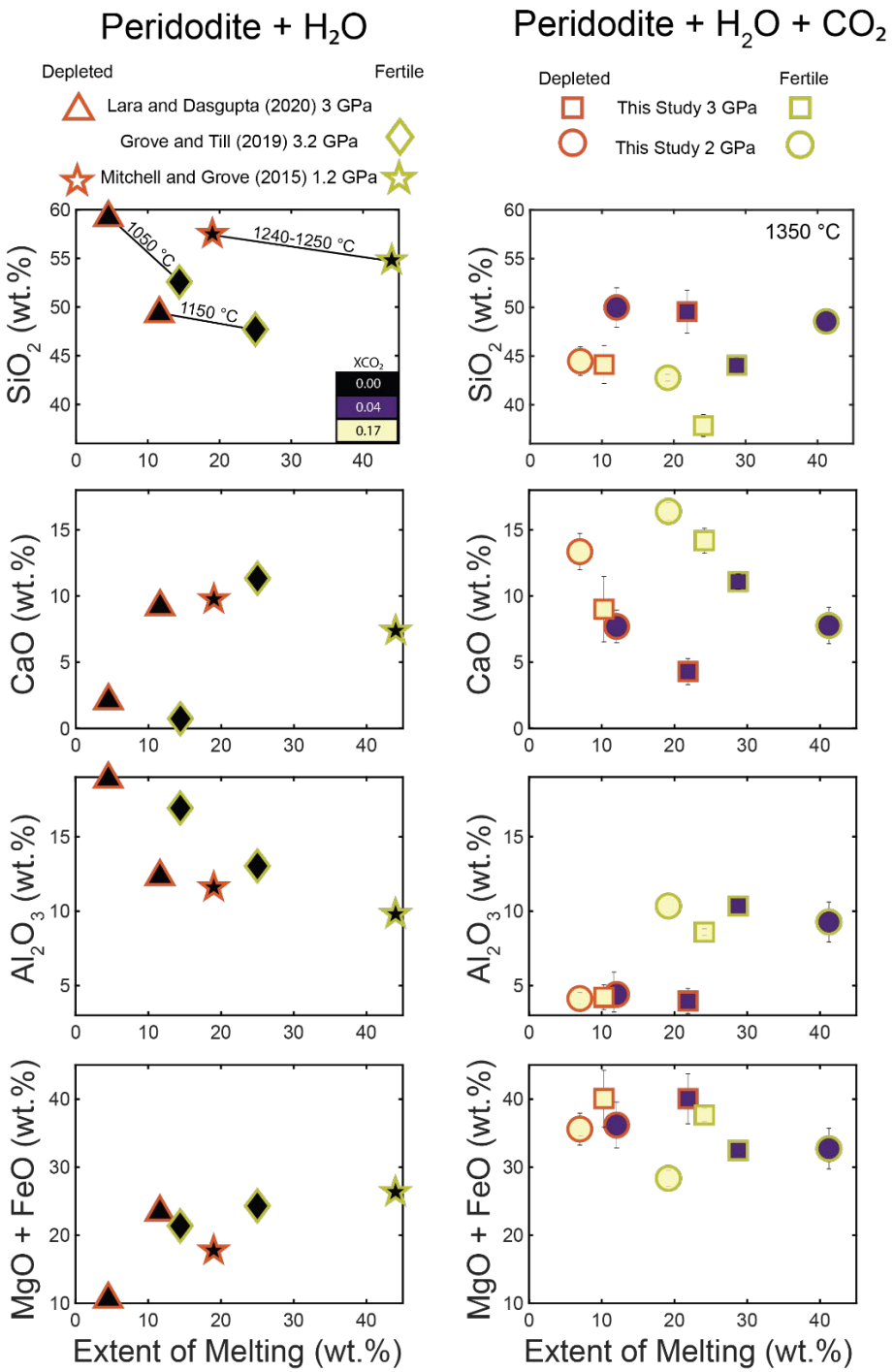

Figure 9. Major element compositions of experimental partial melts plotted on a volatile-free basis from this study (right panel), the high pressure depleted and fertile peridotite + H_2O studies of Lara & Dasgupta (2020), Grove & Till (2019) and Mitchell & Grove (2015) (left panel) all plotted as a function of extent of melting. Each data point is filled according to the XCO_2 of the starting compositions with black data points representing CO_2-free hydrous peridotite experiments. Black lines connect fertile and depleted peridotite experiments run at near identical P-T. Vertical error bars on data are ±1σ uncertainties based on replicate microprobe analyses, as given in Table 3.

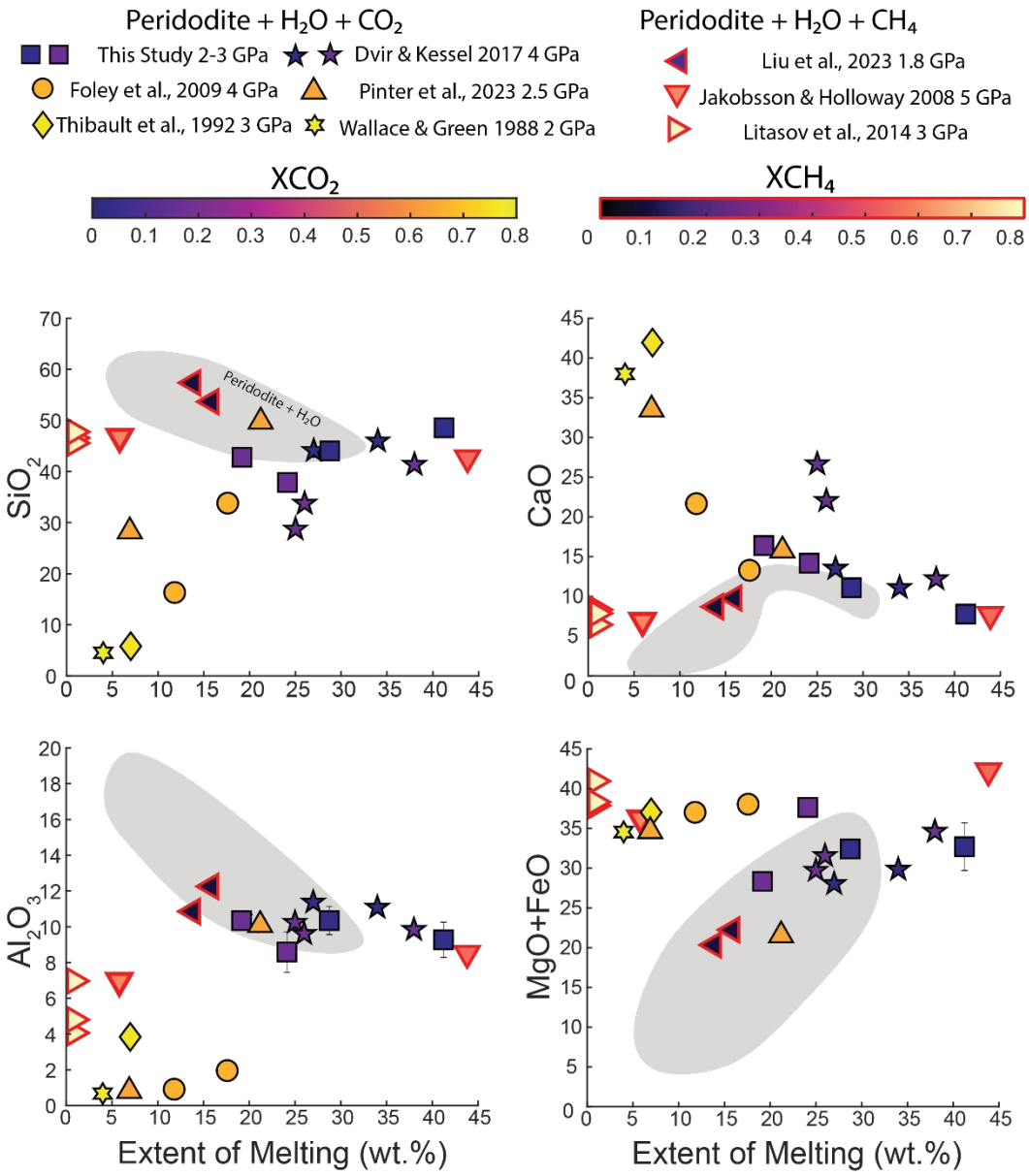

Figure 10. Major element compositions of fertile peridotite experimental partial melts plotted on volatile free bases as a function of extent of melting. The data are separated into partial melts derived from oxidized peridotite + H_2O + CO_2 experiments and reduced peridotite + H_2O + CH_4 experiments as indicated by the color bars, which represent the XCO_2 or XCH_4 of the starting compositions from which the partial melts are derived. The gray field represents the compositional space of partial melts from fertile peridotite + H_2O experiments compiled from the studies by Grove and Till (2019), Tenner et al., (2012), Mitchell and Grove (2015), and Pirard and Hermann (2015). Vertical error bars on data are ±1σ uncertainties based on replicate microprobe analyses, as given in Table 3.

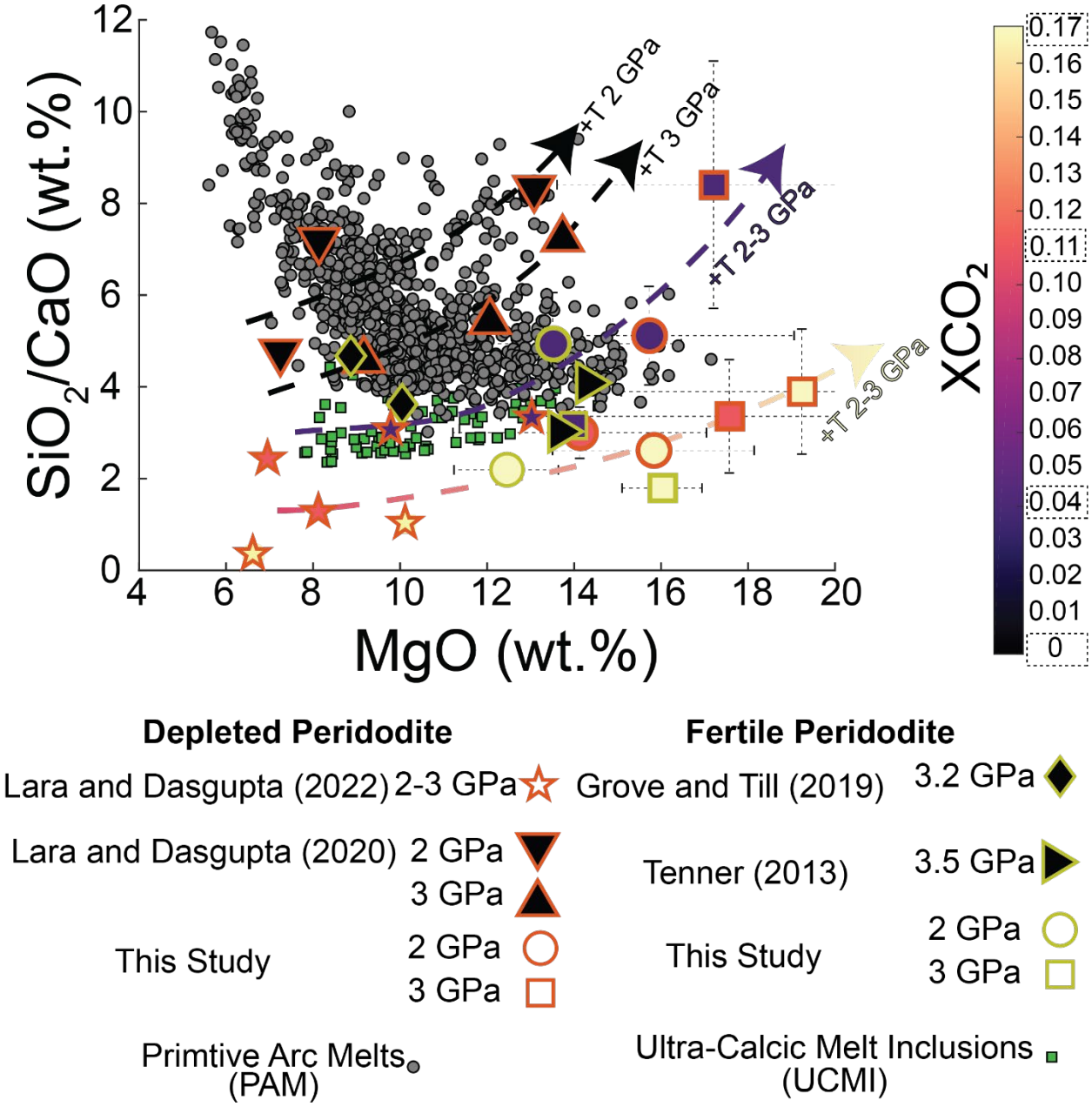

Figure 11. SiO_2/CaO weight ratios vs MgO of fractionation corrected experimental partial melts from this study, the depleted peridotite + H_2O + CO_2 study of Lara and Dasgupta (2022), the depleted peridotite + H_2O study of Lara and Dasgupta (2020) and the fertile peridotite + H_2O studies of Tenner et al. (2013) and Grove and Till (2019). All experimental melts are plotted on a volatile-free basis and compared to primitive arc melts from Schmidt and Jagoutz (2017) and ultra-calcic melt inclusions (Kamenetsky and Clocchiatii 1996; Schiano 2000; Kamenestsky et al., 2007; Elburg et al. 2007; Sorbadere et al. 2011). Data points are filled according to the color bar and dotted bounding boxes around the numbers next to the color bar represent the XCO_2 of experiments plotted. Vertical error bars on experimental melts from this study are ±1σ uncertainties based on replicate microprobe analyses, as given in Table 3. Note that all bulk

compositions with $XCO_2 > 0.04$ from 1200 – 1350 °C produce melts with lower SiO_2/CaO than all primitive arc melts.

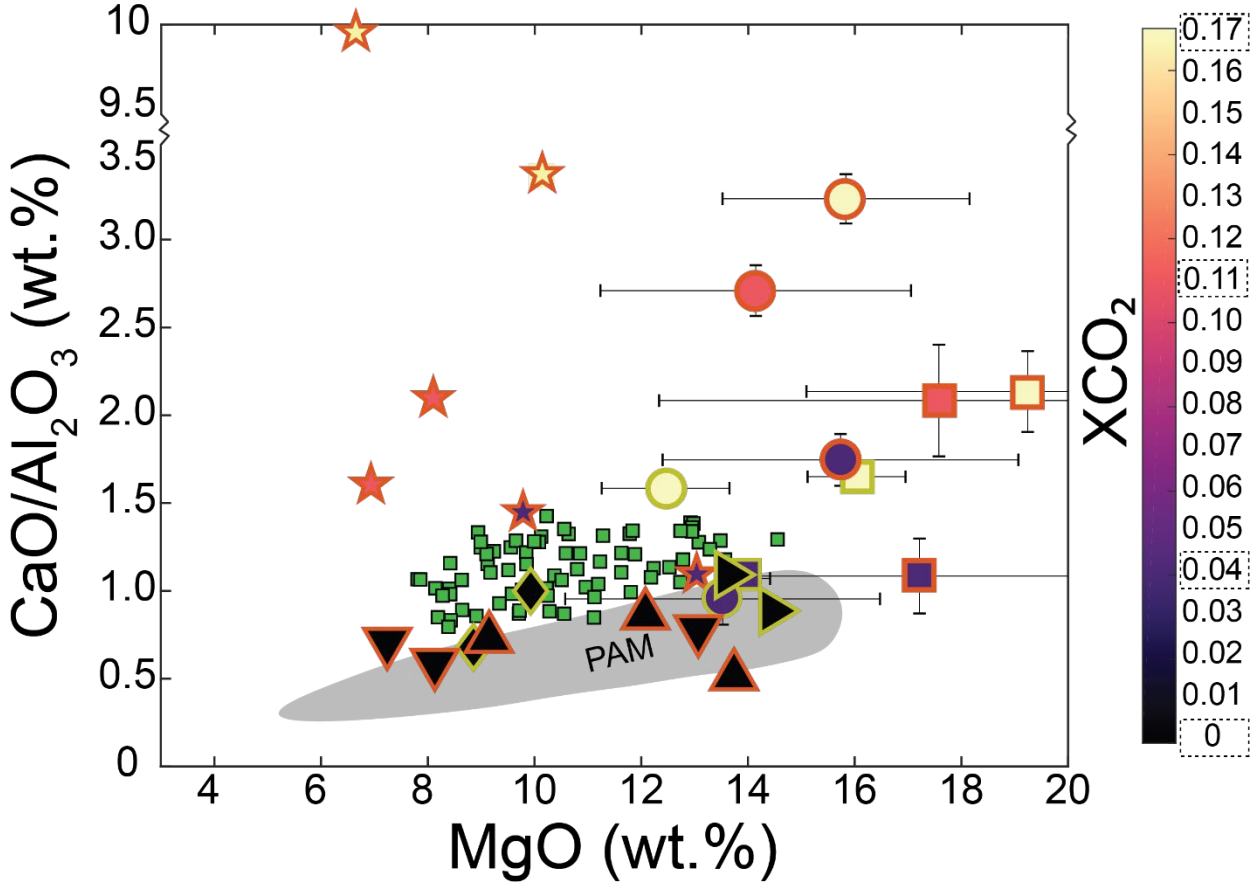

Figure 12. CaO/Al_2O_3 ratios of fractionation corrected experimental melts as shown in Figure 10 plotted as a function of MgO content. All experimental melts are plotted on a volatile-free basis and compared to ultra-calcic melt inclusions (UCMIs; green squares, from Kamenetsky and Clocchiatii 1996; Schiano 2000; Kamenestsky et al., 2007; Elburg et al. 2007; Sorbadere et al. 2011). Grey field is the CaO/Al_2O_3 – MgO space covered by the global range of primitive arc melts (PAM) from Schmidt and Jagoutz (2017). Data points are filled according to the color bar and dotted bounding boxes around the numbers against the color bar represent the XCO_2 of experiments plotted. Vertical error bars on data are ±1σ uncertainties based on replicate microprobe analyses, as given in Table 3.

Table 1: Compositions of starting materials in this study and previous peridotite + H_2O ± CO_2 melting studies

Study	Kepezhinskas et al. (1995)	Davis et al. (2009)	This Study	This Study	Lara and Dasgupta (2020)	Grove and Till (2019)	Tenner et al. (2013)	Mitchell and Grove (2015)	Mitchell and Grove (2015)
Mix	AVX-51[A]	KLB-1	DP.04, DP.10, DP.17	FP.04, FP.17	DP + 10% MM	Wet H&Z + SM	Batch 2	F	C
Fertility	Depleted	Fertile	Depleted	Fertile	Depleted	Fertile	Fertile	Depleted	Fertile
SiO_2	45.47	44.84	45.47	44.84	47.55	46.3	44.92	44.06	46.31
TiO_2	0	0.11	0	0.11	0.06	0.18	0.16	0.08	0.18
Al_2O_3	0.71	3.51	0.71	3.51	1.37	4.21	3.92	2.17	4.21
Cr_2O_3	0	0.32	0	0.32	0	0.4	0.28	0.45	0.4
FeO*	7.59	8.20	7.59	8.20	7.25	7.48	8.09	8.04	7.48
MnO	0.12	0.12	0.12	0.12	0.11	0.1	0.12	0.12	0.1
MgO	44.82	39.52	44.82	39.52	41.93	37.18	38.76	42.1	37.18
CaO	0.93	3.07	0.93	3.07	0.97	3.2	3.79	1.99	3.2
Na_2O	0.32	0.30	0.32	0.30	0.72	0.59	0.25	0.59	0.59
K_2O	0.04	0.02	0.04	0.02	0.04	0.15	0.03	0.13	0.15
Sum	100	100	100	100	100	99.79	100.32	99.73	99.8
CO_2	0	0.00	0.35, 1.05, 1.75	0.35, 1.75	0	0	0	0	0
H_2O	0	0.00	3.5	3.50	3.5	4.21	2.5	?	3.19
XCO_2	-	-	0.04, 0.11, 0.17	0.04, 0.17	0	0	0	0	0
$CaO+Al_2O_3$	1.64	6.58	1.64	6.58	2.34	7.41	7.71	4.16	7.41
Mg#	91.32	89.57	91.32	89.57	91.16	89.86	89.52	90.32	89.86

Fertile compositions are defined by $CaO+Al_2O_3 > 5$ wt.%, Mg# < 90

Depleted compositions are defined by $CaO+Al_2O_3 < 5$ wt.%, Mg# > 90

FeO* Total ferric and ferrous iron content

? H_2O content of starting mix not reported

Table 2: Experimental conditions, phase assemblages, and available phase proportions of peridotite + H_2O + CO_2 partial melting at 1350 °C.

Exp. No	*P* (GPa)	XCO_2	Duration (h)	Ol	Opx	Melt	∑r^2	%Fe loss
Depleted Peridotite								
B516	2	0.04	91	64.8 (7)	23 (1)	12.0 (6)	0.11 (3)	16.46
B505	2	0.1	95	74 (1)	19 (1)	7.1 (2)	0.22 (3)	27.25
B512	2	0.17	139	64.0 (7)	28.9 (6)	7.1 (2)	0.30 (4)	17.48
B534	3	0.04	70	64 (2)	14 (1)	22 (1)	0.09 (4)	1.89
B517	3	0.1	73	60 (2)	28 (2)	12 (1)	0.11 (7)	18.69
B536	3	0.17	71	64 (2)	26 (1)	10.3 (5)	0.09 (3)	19.36
Fertile Peridotite								
B545	2	0.04	70	54.5 (6)	4 (1)	41 (1)	0.13 (9)	6.2
B513	2	0.17	93	52 (1)	29 (2)	19.2 (5)	0.15 (6)	0.7
B530	3	0.04	69	53 (2)	19 (1)	28.8 (4)	0.03 (1)	11.3
B515	3	0.17	92	42 (1)	34 (1)	24.1 (6)	0.17 (6)	10.8

Experiments are arranged, first for depleted peridotite experiments and second for fertile peridotite experiments. For a given set, experiments are arranged in the order of increasing pressure and at each pressure in order of increasing XCO_2 of the starting compositions. All experiments are conducted using $Au_{75}Pd_{25}$ capsule and at 1350 °C. Numbers in parentheses are the ±1σ determined by propagating errors in each oxide by Monte Carlo simulations (n = 10). For example, 74 (1) should be read as 74 ± 1 wt.% and 64.8 (7) as 64.8 ± 0.7 wt.%. Ol-olivine, Opx = orthopyroxene. $\sum r^2$ is the sum of squared residuals and provide assessments for the quality of mass balance calculations.

Table 3: Partial Melt Compositions

Experiment	B516	B505	B512	B534	B517	B536	B545	B513	B530	B515
P	2	2	2	3	3	3	2	2	3	3
T	1350	1350	1350	1350	1350	1350	1350	1350	1350	1350
XCO_2	0.04	0.11	0.17	0.04	0.11	0.17	0.04	0.17	0.04	0.17
% Fe Loss	16.46	27.25	17.48	2.5	18.69	19.36	6.2	0.7	11	10.8
Method	Fe Corr[A]	Fe Corr	Fe Corr	Measured[B]	Fe Corr	Fe Corr	Fe Corr	Measured	Fe Corr	Fe Corr
n[C]	24	14	19	12	12	16	17	20	26	18
Melt %	12.0 (6)	7.1 (2)	7.1 (2)	22 (1)	12 (1)	10.3 (5)	41 (1)	19.2 (5)	28.8 (4)	24.1 (6)
SiO_2	50 (2)	47 (1)	44 (1)	50 (2)	44 (2)	44 (2)	49 (1)	42.8 (3)	44.0 (8)	38 (1)
TiO_2	-	-	-	-	-	-	0.23 (5)	0.50 (5)	0.30 (5)	0.37 (5)
Al_2O_3	4.4 (6)	4.9 (4)	4.1 (4)	4.0 (8)	5 (1)	4.2 (8)	9 (1)	10.3 (5)	10.4 (3)	8.6 (2)
Cr_2O_3	-	-	-	-	-	-	0.39 (5)	0.16 (4)	0.34 (5)	0.25 (6)
FeO*	11.8 (5)	11.2 (7)	12.0 (4)	12.2 (8)	13 (1)	14.3 (5)	10.4 (5)	10.0 (2)	10.8 (4)	11.6 (3)
MnO	0.23 (3)	0.3 (4)	0.15 (3)	0.25 (4)	0.39 (5)	0.18 (4)	0.15 (2)	0.17 (3)	0.16 (4)	0.20 (4)
MgO	24 (3)	20 (3)	23 (2)	28 (4)	27 (5)	26 (4)	22 (3)	18 (1)	21.6 (4)	26.0 (9)
CaO	8 (1)	13 (2)	13 (1)	4 (1)	10 (2)	9 (2)	8 (1)	16.4 (7)	11.1 (6)	14.2 (9)
Na_2O	1.0 (2)	1.9 (3)	1.7 (6)	1.2 (3)	1.5 (5)	1.8 (7)	0.8 (3)	1.28 (8)	1.1 (3)	0.9 (2)
K_2O	0.5 (1)	0.5 (2)	0.6 (1)	0.7 (2)	0.5 (2)	0.7 (2)	0.2 (1)	0.03 (2)	0.2 (1)	0.06 (5)
Total	100.00	100.00	100.00	100.00	100.00	100.00	100.00	100.00	100.00	100.00
Mg#[D]	0.79	0.77	0.78	0.80	0.79	0.76	0.79	0.77	0.78	0.80
Kd[E]	0.29	0.29	0.30	0.28	0.31	0.28	0.28	0.31	0.31	0.32

Melt compositions are reported on a volatile-free basis. ±1σ error in parentheses, based on replicate electron microprobe analyses, are reported as least digits cited. For example, 50 (2) should be read as 50 ± 2 wt.% and 4.4 (6) as 4.4 ± 0.6 wt.%.

[A] Fe-Corr columns report melt compositions corrected for Fe loss to metal capsules.

[B] Measured melt compositions.

[C] *n* = number of EPMA spot analyses averaged to obtain the reported melt composition.

[D] Mg# = [molar MgO/(molar MgO + molar FeO*)]×100

[E] $Kd^{ol}_{melt} = \frac{X^{ol}_{Feo}}{X^{Melt}_{FeO}} \times \frac{X^{Melt}_{MgO}}{X^{Ol}_{MgO}}$ Using measured melt and olivine compositions.

FeO* Total ferric and ferrous iron content